The influence of gas pore pressure in dense granular flows: numerical simulations versus experiments and implications for pyroclastic density currents

Alvaro Aravena, Laurent Chupin, Thierry Dubois, Olivier Roche

1 **The influence of gas pore pressure in dense granular flows: numerical simulations versus**

2 **experiments and implications for pyroclastic density currents**

3 Alvaro Aravena[1,2], Laurent Chupin[2], Thierry Dubois[2], Olivier Roche[1]

4 [1]Laboratoire Magmas et Volcans, Université Clermont Auvergne, CNRS, IRD, OPGC,

5 Clermont-Ferrand, France.

6 [2]Laboratoire de Mathématiques Blaise Pascal, Université Clermont Auvergne, CNRS,

7 Clermont-Ferrand, France.

8 Corresponding author: Alvaro Aravena (alvaro.aravena@uca.fr).

9 **Abstract**

10 We investigate the influence of gas pore pressure in granular flows through numerical

11 simulations on horizontal and low-angle inclined surfaces. We present a two-phase formulation

12 that allows description of dam-break experiments considering high-aspect-ratio collapsing

13 columns and depth-dependent variations of flow properties. The model is confirmed by

14 comparing its results with data of analogue experiments. The results suggest that a constant,

15 effective pore pressure diffusion coefficient can be determined in order to reproduce reasonably

16 well the dynamics of the studied dam-break experiments, with values of the diffusion

17 coefficient consistent with experimental estimates from defluidizing static columns. The

18 discrepancies between simulations performed using different effective pore pressure diffusion

19 coefficients are mainly observed during the early acceleration stage, while the final deceleration

20 rate, once pore pressure has been dissipated, is similar in all the studied numerical experiments.

21 However, these short-lasting discrepancies in the acceleration stage can be manifested in large

22 differences in the resulting run-out distance. We also analyze the pore pressure at different

23 distances along the channel. Although our model is not able to simulate the under-pressure

24 phase generated by the sliding head of the flows in experiments and measured beneath the flow-

25 substrate interface, the spatio-temporal characteristics of the subsequent over-pressure phase

26 are compatible with experimental data. Additionally, we studied the deposition dynamics of the

27 granular material, showing that the timescale of deposition is much smaller than that of the

28 granular flow, while the time of the deposition onset varies as a function of the distance from

29 the reservoir, being strongly controlled by the surface slope angle. The simulations reveal that

30 an increment of the surface slope angle from 0° to 10° is able to increase significantly the flow

31 run-out distance (by a factor between 2.05 and 2.25, depending on the fluidization conditions).

32 This has major implications for pyroclastic density currents, which typically propagate at such

33 gentle slope angles.

34

1. Introduction

36 Pyroclastic density currents (PDCs) are gravity-driven flows of hot particles (pyroclasts and

37 lithic fragments) and gas (Druitt 1998; Branney and Kokelaar 2002; Dufek et al. 2015; Dufek

38 2016) generated by the partial or total collapse of an eruptive column or a volcanic dome. They

39 exhibit a wide range of particle concentration, temperature and grain size distribution, and two

40 physical regimes can be recognized as end-members (Branney and Kokelaar 2002; Burgisser

41 and Bergantz 2002; Dufek 2016): dilute and dense flows, which may occur alone (e.g. dilute

42 turbulent flow) or simultaneously (e.g. dense base and overriding turbulent part) during the

43 propagation of a PDC. The dilute component of PDCs consists in a turbulent suspension with

44 a solid concentration of the order of 1 vol. % or less dominated by the interaction between solid

45 particles and the interstitial gas, while the dynamics of the dense component of PDCs, if present,

46 is typically dominated by particle-particle interaction and by friction with the topography,

47 presenting a solid concentration of the order of 30 – 60 vol. % (Lube et al. 2020). A transport

48 regime of PDCs characterized by clusters at intermediate particle concentrations (i.e., a few

49 vol.% to ~30 vol.%) has been recognized recently and may be present for instance in a

50 transitional zone between a dense base and an upper dilute turbulent part (Breard et al. 2016;

51 Fullmer and Hrenya 2017; Lube et al. 2020). Because of their high propagation velocities,

52 dynamic pressures and temperatures, PDCs can devastate urbanized zones, being one of the

53 most hazardous processes associated with volcanic eruptions (Druitt 1998; Branney and

54 Kokelaar 2002; Cole et al. 2015; Neri et al. 2015). Thus, deciphering the factors controlling

55 their dynamics and the expected run-out distance is of paramount importance for volcanic

56 hazard assessment. Although much attention has been paid to the study of the long run-out

57 distance that characterize some PDCs (Bursik and Woods 1996; Branney and Kokelaar 2002;

58 Kelfoun 2011; Roche et al. 2016, 2021; Shimizu et al. 2019; Giordano and Cas 2021), several

59 aspects remain poorly understood. PDC run-out distance is the result of a series of concomitant

60 processes whose relative efficiency is influenced by the flow properties (e.g. solid particle

61 concentration, volume, speed and temperature) and the regional slope (Valentine et al. 2011),

62 and include: the interaction with the surrounding atmosphere (e.g., air entrainment and heat

63 transfer; Benage et al. 2016), the rheological effect of interstitial pore fluid pressure (Druitt et

64 al. 2007; Roche 2012), and the interplay between the flow base and the substrate, where

65 different processes may occur, such as erosion (Cas et al. 2011; Bernard et al. 2014; Farin et al.

66 2014), self-channelization (Brand et al. 2014; Gase et al. 2017), self-fluidization (Breard et al.

67 2018; Chédeville and Roche 2018), and pyroclast deposition (Branney and Kokelaar 2002).

68 In particular, within the pyroclastic mixture, and especially at the impact zone of a collapsing

69 fountain (Sweeney and Valentine 2017; Valentine and Sweeney 2018; Valentine 2020; Fries et

70 al. 2021), the differential motion between the interstitial gas (flowing relatively upwards) and

71 the solid particles (moving relatively downward) is able to generate pore pressure, which

72 counterbalances the weight of the particles, reduces friction and thus increases run-out distance

73 (Iverson 1997; Savage and Iverson 2003; Goren et al. 2010; Roche 2012; Rowley et al. 2014;

74 Breard et al. 2019a). The temporal evolution of pore pressure, and thus its effective influence

75 on run-out distance, depends on the balance between some source mechanisms (e.g. gas

76 ingestion, differential gas-particle motion caused by particle settling) and pore pressure

77 diffusion, which is in turn controlled by the properties of the PDC material. In fact, slow gas

78 pressure diffusion is favored by thick pyroclastic flows and by grain size distributions

79 dominated by fine particles that confer low hydraulic permeability (Druitt et al. 2007; Burgisser

80 2012; Roche 2012; Breard et al. 2019b).

81 In this work we address the influence of pore pressure on the propagation of granular flows

82 through numerical simulations. In particular, we present a two-phase model, built on the

83 formulation presented by Chupin et al. (2021), which accounts for the effect of pore pressure

84 on the dynamics of granular flows and allows us to simulate collapsing columns in the dam-

85 break configuration and the subsequent flow propagation on horizontal and low-angle inclined

86 surfaces. The column height and aspect ratio adopted in our numerical simulations (40 cm and

87 2, respectively) were selected to allow model confirmation by comparing numerical results with

88 published experimental data (cf. Valentine 2019; Esposti Ongaro et al. 2020) of collapsing

89 columns over a horizontal surface (Roche et al. 2010). Note that we use the term *confirmation*

90 instead of *validation* following the framework presented by Esposti Ongaro et al. (2020).

91 Numerical results also allow us to explore some key physical aspects controlling the dynamics

92 of granular flows (e.g. pore pressure spatio-temporal evolution and flow deposition), which are

93 often difficult to measure in time across the entire spatial domain of analogue experiments.

94 Moreover, adopting a set of input conditions calibrated using experimental data, we performed

95 additional simulations considering collapsing columns on low-angle inclined rigid surfaces, in

96 order to test the coupled effect of pore pressure and topography on the propagation of granular

97 flows. Compared to previous efforts to address numerically the influence of pore pressure in

98 the propagation dynamics of PDCs (Gueugneau et al. 2017), which are based on depth averaged

99 models, our model has some relevant strengths: it allows us to study high-aspect ratio collapsing

100 columns and to describe depth-dependent variations of the flow properties.

This article consists of five sections. In Section 2 we describe the experimental configuration considered in this paper. In Section 3, we present the numerical model adopted (Section 3.1), its confirmation by comparing numerical results with those of analogue experiments (Section 3.2), and then we describe the results of simulations performed considering low-angle inclined surfaces (Section 3.3). Finally, in Sections 4 and 5 we present the discussion and concluding remarks of this article.

2. Experimental configuration

In order to test and confirm our model, we considered the experimental data presented by Roche et al. (2010). The benchmark experiment consists in the release of a fluidized granular column into a horizontal, smooth channel (note that the term *fluidization* is used here to refer to the presence of a vertical flow of air able to counterbalance the bed weight, and it is not related to the presence of other fluid phases such as water). The dynamics of the dam-break experiment, which was measured using high-speed cameras and pressure sensors located at different positions along the horizontal channel, can be decomposed into three stages: (1) a quick phase of initial acceleration, (2) propagation of the front at nearly constant velocity, and (3) deceleration of the flow and front stopping. Roche et al. (2010) and Chupin et al. (2021) also pointed out a final stage of very slow propagation of granular material in the flow body after the front stopped. The experimental apparatus includes a reservoir of 20 cm length and 10 cm width, and a channel of 3 m length and 10 cm width. Initially, the particles are introduced into the reservoir (column height of 40 cm) where an air flow is supplied from below in order to generate fluidization and the related pore pressure. This simple configuration aims to mimic particle-gas differential motion generated through various means, including particle settling (Chédeville and Roche 2018; Breard et al. 2018; Valentine and Sweeney 2018; Fries et al. 2021). Roche et al. (2010) tested two fluidization conditions by adjusting the supplied air

126   velocity: (1) imposing the minimum fluidization velocity (U_{mf}) or (2) imposing the minimum

127   bubbling velocity (U_{mb}). The minimum fluidization velocity U_{mf} (~ 0.8 cm/s in the

128   experiments; Roche et al. 2010) guaranties that the bed weight is counterbalanced by the drag

129   of the interstitial air flow on the particles, and the granular bed is not expanded. On the other

130   hand, at U_{mb} (~ 1.3 cm/s in the experiments; Roche et al. 2010), the bed weight is

131   counterbalanced and the granular network is expanded. In order to trigger column collapse, at

132    $t = 0$, a sluice gate is opened rapidly ($< \sim 0.1$ s), allowing to release the granular material,

133   which propagates laterally along the horizontal channel during about 1.3 s. As our numerical

134   model treats incompressible flows, we compare our results with the analogue experiment

135   performed using the minimum fluidization velocity (U_{mf}), that is, when the bed is not

136   expanded. The particles used in these experiments were spherical glass beads with a grain size

137   range of 60-90 µm (monodisperse size distribution, mean of 75 µm) and a density of $\rho_s =$

138   2500 kg/m^3. Note that more complex particle shapes and size distributions are able to control

139   pore pressure diffusion in granular flows by affecting porosity and mixture permeability

140   (Wilson 1984; Burgisser 2012; Breard et al. 2019b and references therein), and that Breard et

141   al. (2019b) showed that the effective particle size regarding fluidization and pore pressure

142   diffusion is the Sauter diameter, which is very close to the mean diameter for subspherical

143   particles such as we considered. The resulting granular column had a bulk density of $\rho_b =$

144   1450 ± 50 kg/m^3 (i.e. pore volume fraction of $\varepsilon = 0.42 \pm 0.02$). Additionally, we can

145   calculate the theoretical hydraulic diffusion coefficient $\kappa_T = k/(\varepsilon\mu\beta)$, where k is hydraulic

146   permeability, μ is gas dynamic viscosity and β is gas compressibility. In case of a perfect gas,

147    $\beta = 1/P_i$, where P_i is the initial pore pressure, which is about equal to the atmospheric pressure.

148   Considering that $k \sim 10^{-11}$ m^2, $\varepsilon \sim 0.42$, and $\mu \sim 1.8 \times 10^{-5}$ Pa s, we obtain $\kappa_T \sim 0.13$ m^2/s.

149   However, it is worth noting that this value is one order of magnitude larger than the estimates

150   of diffusion coefficient given by Roche et al. (2010) ($\kappa \sim 0.01$ m^2/s), which are based on

151   experimental measurements on static defluidizing beds and are shown to increase with the bed

152   height. The reason explaining this discrepancy is unknown and is discussed below.

153

154   **3.   Numerical simulations**

155   **3.1 Mathematical modelling and numerical schemes**

156   Based on the numerical model presented by Chupin et al. (2021), we constructed a new model

157   able to consider the effect of pore pressure and reproduce the experimental configuration

158   adopted by Roche et al. (2010). We consider the collapse of a granular mass over a planar rigid

159   surface with inclination angle θ varying from horizontal up to 10°. As the laboratory

160   experiments have been performed in a narrow channel (10 cm wide and 3 m long; Roche et al.

161   2010), we consider the problem as mainly two-dimensional. Note that we neglect the effects of

162   the lateral walls.

163   The granular medium, which is a mixture of air and glass beads, is described by an

164   incompressible flow with a µ(I)-rheology (Jop et al. 2006). In this rheological model, which

165   has been widely adopted to describe dense granular flows (Gray and Edwards 2014; Ionescu et

166   al. 2015), the dynamics of the granular flow is governed by the mass and momentum

167   conservation laws

$$\rho(\partial_t \boldsymbol{u} + \boldsymbol{u} \cdot \nabla \boldsymbol{u}) = \operatorname{div} \boldsymbol{T} + \rho \boldsymbol{g}, \tag{1}$$

$$\operatorname{div} \boldsymbol{u} = 0, \tag{2}$$

$$\partial_t \rho + \boldsymbol{u} \cdot \nabla \rho = 0, \tag{3}$$

168

169   where $\boldsymbol{u}$ is the material velocity, $\boldsymbol{g}$ is an external force (gravity), $\boldsymbol{T}$ is the total stress tensor, and

170    $\rho = \phi \rho_s$ is the bulk density, where ρ_s and ϕ are the particle density and average volume

171   fraction, respectively. In our simulations, based on the experimental data described by Roche

172   et al. (2010), we use $\rho_s = 2500 \text{ kg/m}^3$ and $\phi = 1 - \varepsilon = 0.58$. The pressure is given by $p =$

173      $-\frac{1}{3}\text{tr}\,\boldsymbol{T}$, so that the deviatoric stress $\boldsymbol{T}'$ ($\boldsymbol{T} = -p\boldsymbol{Id} + \boldsymbol{T}'$) has to be prescribed in order to close

174   equations (1) – (3).

175   Modeling the granular flow with equations (1) – (3) entails that the total pressure p is the sum

176   of the solid (effective) pressure p_s, due to force chains of glass beads, and the pore pressure p_f,

177   due to the presence of air between particles. Therefore, in order to account for the presence of

178   air between glass beads, the pore pressure and its effect on granular flows should be modeled.

179   Following Iverson and Denlinger (2001), the pore pressure diffuses and is advected with the

180   granular mass so that p_f satisfies the balance equation

$$\partial_t p_f - \text{div}(\kappa \nabla p_f) + \boldsymbol{u} \cdot \nabla p_f = 0, \tag{4}$$

181   where κ is the diffusion coefficient. The knowledge of p_f through equation (4) permits us to

182   define the effective pressure as $p_s = p - p_f$.

183   In the μ(I)-rheology (Jop et al. 2006), the deviatoric stress $\boldsymbol{T}'$ is given by

$$\boldsymbol{T}' = \mu(I) p_s \frac{\boldsymbol{D}(\boldsymbol{u})}{|\boldsymbol{D}(\boldsymbol{u})|}, \tag{5}$$

184

185   where $\boldsymbol{D}(\boldsymbol{u}) = \frac{1}{2}(\nabla \boldsymbol{u} + \nabla \boldsymbol{u}^t)$ is the strain rate tensor and $|\boldsymbol{D}(\boldsymbol{u})|^2 = \frac{1}{2}\sum_{i,j} \boldsymbol{D}(\boldsymbol{u})_{i,j}^2$. The friction

186   coefficient $\mu(I)$ depends on the inertial number I, namely

$$\mu(I) = \mu_s + \frac{\mu_\infty - \mu_s}{1 + I_0/I} \text{ and } I = \frac{2d|\boldsymbol{D}(\boldsymbol{u})|}{\sqrt{p_s/\rho_s}}. \tag{6}$$

187   In equation (6), d is the particle diameter, I_0 is a dimensionless number, $\mu_s = \tan(\alpha)$ with α

188   representing the static internal friction angle of the granular material, and $\mu_\infty \geq \tan(\alpha)$ is an

189   asymptotic value of the friction coefficient for large inertial numbers. By combining equation

190   (6) and equation (5) (see Chupin et al. (2021) for the details), we can rewrite the expression of

191   the tensor $\boldsymbol{T}'$ in regions where $\boldsymbol{D}(\boldsymbol{u}) \neq 0$ as

$$\boldsymbol{T}' = 2\eta(|\boldsymbol{D}(\boldsymbol{u})|, p_s)\boldsymbol{D}(\boldsymbol{u}) + \tan(\alpha)\, p_s \frac{\boldsymbol{D}(\boldsymbol{u})}{|\boldsymbol{D}(\boldsymbol{u})|}, \tag{7}$$

192   with

$$\eta(|\boldsymbol{D}(\boldsymbol{u})|, p_s) = \frac{(\mu_\infty - \tan(\alpha))p_s}{2|\boldsymbol{D}(\boldsymbol{u})| + \frac{I_0}{d}\sqrt{p_s/\rho_s}}. \tag{8}$$

193   With this formulation, the μ(I)-rheology appears to be a viscoplastic rheology with a Drucker-

194   Prager plasticity criterion (see also Jop et al. 2006 and Ionescu et al. 2015) and a spatio-temporal

195   variable viscosity, which is a fundamental aspect of our study. In order to treat the non-

196   differentiable definition of the tensor $\boldsymbol{T}'$, due to the presence of the $1/|\boldsymbol{D}(\boldsymbol{u})|$ term that is

197   singular in the absence of strain rate, a projection scheme is applied (Chalayer et al. 2018;

198   Chupin et al. 2021). The projection procedure avoids a need to resort to any regularization

199   technique and allows to accurately capture the rigid zones, i.e., the regions where no

200   deformation occurs.

201   As in Chupin et al. (2021), the presence of the ambient gas (i.e. the air outside the flow) is taken

202   into account. The granular flow and the ambient air flow are separated by an interface

203   transported by the velocity field. A level-set function Φ (see Osher and Fedkiw (2001) for

204   instance), initially defined as the signed distance to the interface, is used to describe the limit

205   between the granular flow and the ambient gas. The computational domain is split so that $\Phi <$

206   0 corresponds to the granular flow, $\Phi > 0$ the ambient gas and $\Phi = 0$ the interface. The level-

207   set function satisfies the equation

$$\partial_t \Phi + \boldsymbol{u} \cdot \boldsymbol{\nabla}\Phi = 0. \tag{9}$$

208   The ambient flow ($\Phi > 0$) is also governed by equations (1) – (3) but with a Newtonian

209   rheology, namely $\boldsymbol{T}' = 2\eta_f \boldsymbol{D}(\boldsymbol{u})$ where η_f is the air dynamic viscosity, and a mass density $\rho =$

210   ρ_f. Note that the pore pressure equation (4) has a meaning only inside the granular flow, that is

211   where $\Phi < 0$. In order to solve an equation valid over the whole computational domain, the

212   diffusion coefficient κ takes a very large value ($\approx 10^{16}$ m^2/s) outside the granular flow so that

213   p_f is extended to zero outside of the granular flow.

214   Coulomb friction boundary conditions are applied on the vertical backwall of the reservoir and

215   on the bottom of the channel on which the granular medium slides, that is

$$u_n = 0 \text{ and } \boldsymbol{T}_t = -\eta_\text{b}\boldsymbol{u}_t - \tan(\alpha_b)\,(-T_n)^+ \frac{\boldsymbol{u}_t}{|\boldsymbol{u}_t|}, \tag{10}$$

216   where $u_n = \boldsymbol{u} \cdot \boldsymbol{n}$ ($\boldsymbol{n}$ being the unit outward normal vector to the domain boundary) is the

217   normal velocity and $\boldsymbol{u}_t = \boldsymbol{u} - u_n\boldsymbol{n}$ the tangential one. Similarly, for the stress we have $T_n =$

218    $(\boldsymbol{T} \cdot \boldsymbol{n}) \cdot \boldsymbol{n}$ and $\boldsymbol{T}_t = \boldsymbol{T} \cdot \boldsymbol{n} - T_n\boldsymbol{n}$. In all simulations reported in this paper, the friction angle on

219   the vertical backwall of the reservoir and on the bottom of the channel (α_b) was set to $15°$

220   (Chupin et al. 2021).

221   At time $t = 0$, the pore pressure p_f is initialized in the reservoir as 90% of the weight of the

222   particles, that is, $p_f(x, y) = 0.9\rho g(H - y)$ (H being the height of the initial column), which

223   agrees with experimental measurements (Montserrat et al. 2012). Equation (4) is supplemented

224   with Neumann boundary conditions. On the bottom of the channel inside the reservoir, that is

225   for $x \in [-20 \text{ cm}, 0 \text{ cm}]$ and $y = 0$, the constant air flux imposed in the experiment is modeled

226   with a constant pressure gradient $\frac{\partial p_f}{\partial n} = -0.9\rho g$. Everywhere else on the domain boundary, a

227   homogeneous Neumann boundary condition $\frac{\partial p_f}{\partial n} = 0$ is applied.

228   Equations (1) – (3) and (4) are discretized in space with second order finite volume schemes on

229   a staggered grid. A bi-projection scheme (Chalayer et al. 2018) is applied for the temporal

230   discretization. The level-set transport equation (9) is solved with a RK3 (third-order Runge-

231   Kutta) TVD (total variation diminishing) scheme coupled with a fifth-order WENO (weighted

232   essentially non-oscillatory) scheme. We also apply a reinitializing algorithm in order to

233   maintain the level-set function to the signed-distance function to the interface between the

234   granular and the ambient flows. Details on the numerical schemes are provided in Chupin and

235   Dubois (2016), Chalayer et al. (2018), and Chupin et al. (2021). In order to remedy to a lack of

236   resolution of the small scale structures outside the granular flow, due to the small value of the

237 air viscosity, a subgrid scale (Smagorinsky) model is used (Smagorinsky 1963). This results in

238 enhancing the viscosity of air η_f by adding a local eddy viscosity defined as $(C_s h)^2 |D(u)|$,

239 where h is the mesh size and $C_s \in [0.1, 0.2]$ is the Smagorinsky constant. We used hereafter

240 the value 0.1 for C_s in all simulations.

241 The code, written in F90, is parallel: the PETSc library (Balay et al. 2018a, 2018b) is used to

242 solve the linear systems and to manage data on structured grids while communications between

243 processes are explicitly written with MPI subroutines.

244 **3.2 Simulations on horizontal planes**

245 As a first step, we performed a set of simulations on horizontal surfaces using the model

246 described in Section 3.1 and considering different values of the pore pressure diffusion

247 coefficient (κ). Here we focus on the results of simulations that agree reasonably well with the

248 experimental results presented by Roche et al. (2010) in terms of run-out distance, temporal

249 evolution of the front position and profile of the flow surface, that is, with pore pressure

250 diffusion coefficients ranging from 0.015 to 0.035 m^2/s. Interestingly, these values agree with

251 those determined experimentally by measuring the timescale of pore pressure diffusion in static

252 columns of heights of ~15-35 cm. For comparison purposes, we also include the results of a test

253 simulation performed using the theoretical hydraulic diffusion coefficient ($\kappa_T \sim 0.13$ m^2/s).

254 Note that we consider constant effective diffusion coefficients (with values of 0.015, 0.025, and

255 0.035 m^2/s), while the diffusion coefficient likely varies during the analogue experiment due to

256 granular material dilation and compaction. To reproduce the initial setup of the benchmark

257 analogue experiment, in our simulations the initial height of the collapsing column is 40 cm and

258 the initial width is 20 cm. The height of the computational domain is 45 cm, adopting a grid

259 with 128 cells in the vertical direction (i.e. cell size of 3.5 mm).

260 Our model tends to under-estimate the deposit thickness in proximal domains (from <5% up to

261 ~25%) and to over-estimate the deposit thickness in distal domains (Figs. 1a-c and 2). Still, the

262 general shapes of the simulated final profiles of the deposits are very similar to that of the

263 benchmark analogue experiment, i.e. profiles dipping gently downstream and with the

264 maximum thickness located in the channel near the reservoir. This deposit shape differs clearly

265 from that of non-fluidized granular flows, whose maximum thickness is located at the back-

266 wall of the reservoir while the thickness decreases monotonically with distance (Roche et al.

267 2010; Ionescu et al. 2015). Moreover, numerical results reproduce reasonably well the three

268 phases of propagation described by Roche et al. (2010) (Fig. 3), and the relative duration of

269 each phase as well as the flow duration are consistent with the benchmark experiment. The

270 dynamics of gate opening in the analogue experiment slightly affects flow propagation during

271 the initial acceleration phase, which may explain the differences in the initial front velocity

272 during about 10% of the simulation duration (Figs. 3). An effective diffusion coefficient (κ) of

273 about 0.015 m^2/s reproduces the experimental run-out distance, whereas a larger values of

274 diffusion coefficient reproduce better the maximum thickness of the deposit. Note that, because

275 our simulations are not able to describe flow thicknesses lower than 3.5 mm (i.e. the cell size

276 used in numerical simulations), we compare our results with filtered experimental data, that is,

277 with no consideration of flow thicknesses below this threshold (see Fig. 3 and its caption). On

278 the other hand, the use of the theoretical value of the diffusion coefficient (i.e. 0.130 m^2/s) fails

279 completely in reproducing the propagation dynamics of the benchmark experiment, under-

280 estimating significantly the run-out distance (<60% of the run-out distance measured in the

281 benchmark experiment; Figs. 1d, 2 and 3).

282 The simulations performed using $\kappa = 0.015$ and $\kappa = 0.035$ m^2/s give rise to differences of

283 about 15% in the maximum velocity reached by the flow front (Fig. 4). The phase of velocity

284 increase lasts ~17-22% of the whole propagation time, while the constant-velocity stage, which

285 is slightly longer for simulations with low diffusion coefficients, represents ~15-25% of the

286 total propagation time. Most of the propagation time of the granular flows (about 60-70%) is

287   associated with the phases of deceleration and front stopping. Our results of maximum velocity

288    $(u/\sqrt{gH} \sim 1.0 - 1.15)$ are consistent with the results presented by Roche et al. (2010), which

289   further confirm the validity of our model. Note that the initial phase is characterized by the

290   same acceleration in all the simulations, and the main differences between our simulations are

291   observed in the absolute duration of this stage (and thus in the velocity reached by the flow

292   front, Fig. 4). Another interesting result is that the velocity decrease during the final phase

293   occurs at a similar rate in all the simulations (deceleration of $\sim 0.23g$). This shows that the

294   differences in the front velocity during early phases of flow propagation are the cause of the

295   different run-out distances, while negligible differences are observed in the dynamics of the

296   deceleration stage. This is consistent with the fact that, once the initial pore pressure is

297   completely dissipated, granular flows have the same rheological behaviour. On the other hand,

298   as observed by Roche (2012), during the stopping stage the run-out distance increases with time

299   to the power of 1/3.

300   The evolution of the pore pressure (Fig. 5) is the result of the coupled effect of diffusion, which

301   occurs at a rate controlled by κ, and advection, controlled by flow velocity and thus in turn

302   influenced by κ. Basal pore pressure undergoes an initial phase dominated by advection (i.e.

303   advance of the iso-pressure fronts, which indicate the position along the x-axis at which specific

304   values of pore pressure are reached as a function of time; Fig. 6), and a later phase dominated

305   by diffusion (i.e. recession of the iso-pressure fronts) until stationary conditions are reached

306   (Fig. 6). In particular, the simulations with $\kappa = 0.025 \text{ m}^2/\text{s}$ and $\kappa = 0.035 \text{ m}^2/\text{s}$ show a

307   smooth, gradual transition between both phases. Instead, some of the iso-pressure fronts (Fig.

308   6) for the simulation with $\kappa = 0.015 \text{ m}^2/\text{s}$ show a significantly longer phase dominated by

309   advection and then an abrupt decrease of pore pressure near the front. This rapid pore pressure

310   decrease is favored by the small thickness of the granular flow at the front, while in the other

311   cases such small flow thicknesses are reached while the flow is already defluidized.

312   In order to further compare our results with experimental data (Roche et al. 2010), we studied

313   the pore pressure signal at different points along the channel base. Note that the under-pressure

314   phase measured in experiments beneath the flow-substrate interface during the passage of the

315   sliding head of the flow cannot be computed in our numerical simulations. Still, in Figure 7a-c

316   we show the evolution of the modeled basal pore pressure at specific points along the x-axis,

317   and we also display the differential pressure measured in the benchmark experiment (in the

318   channel base at $x = 0.2$ m). The experimental data show that the passage of the flow front at a

319   given point is followed by a short under-pressure phase and a later and longer over-pressure

320   phase. Roche et al. (2010) propose that the under-pressure stage is mainly caused by the basal

321   slip boundary condition and possibly by dilatancy processes (Garres-Díaz et al. 2020; Bouchut

322   et al. 2021), which is supported by simulations (Breard et al. 2019a). Moreover, the minimum

323   value reached during the under-pressure phase was empirically correlated to the slip velocity

324   (u_{slip}; Roche 2012). The over-pressure phase would be instead dominated by compaction and

325   advection of pore pressure within the granular flow. Since our model does not consider changes

326   in density, it is not able to describe the effect of dilatancy and compaction, and thus under-

327   pressure cannot be modeled, while the over-pressure phase, which is observed in our numerical

328   simulations, is exclusively a consequence of advection (Fig. 7a-c). The relationship between

329   distance along the x-axis and the maximum basal pore pressure reached is remarkably

330   consistent with experimental data both in the curve shape and in the values measured (Fig. 7d),

331   which further confirms the validity of the description of pore pressure used in our model once

332   the under-pressure phase is finished, suggesting that the effect of compaction is limited

333   compared to pore pressure advection. Note that the absence of dilatancy in our model is likely

334   manifested in an earlier peak of the basal pore pressure than that expected in presence of an

335   initial under-pressure stage (Fig. 7e).

336   Roche (2012) proposed that the basal under-pressure measured at the head of granular flows

337   scales with the square of the flow front velocity. Based on this observation, Breard et al. (2019a)

338   showed that the differential pressure measured in experiments can be given by

$$p_c = p_f - \frac{1}{2}\rho_b\big(u_{\text{slip}}\big)^2 , \tag{11}$$

339   where p_f is the basal pore pressure and ρ_b is the mixture density at the base. The use of this

340   expression and our numerical results show that the temporal evolution of p_c at different

341   positions along the channel is characterized by a short under-pressure phase followed by a

342   longer over-pressure stage in proximal domains ($x < 0.5$ m, Fig. 8a-c), while distal points

343   present only the under-pressure phase (Fig. 8a-c) because most of the pore pressure is already

344   dissipated at these distances from the reservoir. Although the duration of the under-pressure

345   phase of p_c is shorter than that measured in the benchmark experiment, the simulated minimum

346   values, their evolution with distance and the time at which these values are reached are strongly

347   consistent with experimental data (Fig. 8d-e). On the other hand, while the maximum values of

348   p_c and those of experimental data are in agreement, the times at which these maximum values

349   are observed are shifted.

350   The deposition dynamics of particles in the simulations is shown in Figure 9. Note that these

351   results are a direct consequence of the rheological model adopted and no calibrated inputs of

352   sedimentation rate are needed to parametrize the deposition of granular material. The length of

353   the sliding head (L_h, Fig. 9a) was computed considering that sedimentation occurs at the base

354   of the channel when the slip velocity reaches a value lower than 5% of the maximum slip

355   velocity observed during the simulation. On the other hand, the variable A_d (area of material

356   deposited, Fig. 9a) was calculated by considering the modulus of velocity in each cell of the

357   computational grid. In particular, at a given distance from the reservoir, the thickness of the

358   deposit was computed considering all the cells with a velocity modulus lower than 0.1 m/s (i.e.

359   about 5% of the maximum value of the velocity modulus observed during the simulations). Our

360   simulations show maximum lengths of the flow head of the order of 0.85-1.15 m, slightly larger

361   than the experimental estimates of Roche (2012) (i.e. ~0.7 m; Fig. 9b) and twice the values

362   simulated and observed in analogue experiments of dry granular flows of the same dimensions

363   (i.e. 0.4 – 0.5 m; Roche 2012; Chupin et al. 2021). The relationship between L_h/L and L_d/L_f

364   (see Fig. 9a for definition) shows a linear trend, in agreement with experimental data and also

365   with the behaviour of dry granular flows (Roche 2012; Chupin et al. 2021; Fig. 9c). The

366   evolution of the deposit area compared with the normalized time and run-out distance is also

367   consistent with experimental data. Most of the deposition occurrs during the final 40% of the

368   propagation time-span, when the flow front has already travelled more than 80% of the final

369   run-out distance (Fig. 9d-e). The results show that most of the deposition occurs between $t \approx$

370    $4.0\sqrt{H/g}$ and $t \approx 6.0\sqrt{H/g} - 6.5\sqrt{H/g}$ (Fig. 9f-g) and that lowering the pore pressure

371   diffusion coefficient leads to delayed deposition. The position at which the peak of

372   sedimentation rate occurs increases monotonically with time in all the simulations presented,

373   showing slightly S-shaped curves that start in the vicinity of the reservoir and present maximum

374   advance velocities similar in all the cases ($u_{sp}/\sqrt{gH} \sim 1.4$, where u_{sp} is the advance velocity

375   of the position of the deposition rate peak), significantly higher that the flow front velocity (Fig.

376   9f). Thus, our results suggest that the advance of the position of maximum deposition rate is

377   poorly correlated with the behaviour of the flow front. At a given point along the channel, the

378   deposition of particles tends to occur very rapidly (Fig. 9g). In fact, the time elapsed between

379   the deposition of 10% and 90% of the final deposit at a given point is of the order of $0.1\sqrt{H/g}$,

380   one order of magnitude smaller than the granular flow duration (Fig. 9g). Locally, the

381   sedimentation rate reaches peaks of the order of 1 m/s, with mean sedimentation rates of the

382   order of 0.1 m/s. It is worth noting, however, that this constraint of sedimentation rate is strongly

383   influenced by the threshold used to define the deposited portion of the granular flow during its

384   propagation.

3.3 Simulations on inclined planes

In the previous section we showed that the effective diffusion coefficient required to simulate the benchmark analogue experiment (Roche et al. 2010), which is likely variable in time and position, is in the range $\kappa = 0.015 - 0.035 \text{ m}^2/\text{s}$. Considering these values of diffusion coefficient, we investigated the coupled effect of fluidization and topography through an additional set of simulations adopting variable surface slope angles (from $0°$ to $10°$). Additionally, for comparison purposes, we did complementary dam-break simulations considering inclined surfaces and dry flows, using the model described in Chupin et al. (2021). Thereby, simulations results for run-out distance allow quantifying the combined effects of pore pressure and surface slope angle.

The temporal evolution of the front position of dry and fluidized granular flows shows that a small increment of the surface slope angle is able to significantly increase the maximum run-out distance (Fig. 10). For instance, an increment of surface slope from $0°$ to $10°$ is able to increase the modelled run-out distance from $\sim 2H$ to $\sim 4.4H$ for dry granular flows (relative increase of 220%), where H is the initial column height, while an increase from $\sim 3.8H$ to $\sim 8.4H$ was computed for fluidized flows with $\kappa = 0.025 \text{ m}^2/\text{s}$ (relative increase of 220%). Differences in the propagation velocity between dry and fluidized granular flows are evident from early phases of flow propagation (Figs. 10 and 11). On the other hand, as observed in the simulations described in Section 3.2 for granular flows propagating on horizontal surfaces, also on inclined planes the differences between simulations performed with different diffusion coefficients are mainly manifested in the duration of the initial phase of velocity increase (and thus manifested in the maximum front velocity reached by the flow; Fig. 11). Instead, for a given slope angle, the velocity decrease during the final phase occurs at a similar rate for all the fluidized and dry flows simulated (Fig. 11). This is because, once the pore pressure has been dissipated by diffusion, the rheology of all the simulated granular flows is that of dry flows.

410   The deceleration of the flow front is strongly controlled by the slope angle (Fig. 11), ranging

411   from $\sim 0.23g$ (at 0°) to $\sim 0.11g$ (at 10°). This dependency gives rise to significant differences

412   in the modeled run-out distance as a function of surface slope angle for both dry and fluidized

413   flows (Fig. 12).

414   Run-out of simulated flows also shows important aspects of pore pressure and surface slope

415   angle effects (Fig. 12). For the range of diffusion coefficients adopted here, fluidization of the

416   initial source is able to increase the run-out distance between $\sim 1.55H$ ($\kappa = 0.035$ m^2/s, slope

417   angle of 0°) and $\sim 5.15H$ ($\kappa = 0.015$ m^2/s, slope angle of 10°), corresponding to an increase

418   range of the run-out distance between ~165% and ~225%. Interestingly, the relative increase of

419   run-out distance when fluidized granular flows are compared with dry flows is only weakly

420   controlled by the slope angle (Fig. 12c). On the other hand, for given fluidization conditions,

421   we note that an increase of slope angle from 0° to 10° produces an increment of the run-out

422   distance of about 105-125%. This relative increase in the run-out distance is significantly larger

423   than that measured in analogue experiments by Chédeville and Roche (2015) for lower-aspect

424   ratio collapsing columns (0.5-1.0), i.e., ~60% for an increase of slope angle from 0° to 10°. We

425   speculate that this could be a consequence of the slower pore pressure diffusion that characterize

426   taller collapsing columns.

427   The slope angle has a small influence on the maximum basal pore pressure computed at a given

428   distance (Fig. 13). This shows that the evolution of the basal pore pressure is mainly controlled

429   by the effective pore pressure diffusion coefficient. The length of the sliding head increases

430   significantly when granular flows propagate on inclined surfaces (Fig. 14a-c). On the other

431   hand, inclined topographies are able to delay the onset of deposition and reduce the

432   sedimentation rate (Fig. 14d-f). Interestingly, the shape of the curves describing the evolution

433   of the deposit area (Fig. 14d-f) changes when different slope angles are considered. Deposition

434   in flows propagating on horizontal surfaces occurs at a nearly constant rate during almost all

435 the deposition stage (Fig. 14d-f), and the position at which the maximum deposition rate occurs

436 advances at an almost constant velocity (Fig. 14g-i). However, in simulations performed at high

437 slope angles, the initial stage of deposition, characterized by a relatively low sedimentation rate,

438 is accompanied by a relatively slow advance of the position at which the maximum deposition

439 rate occurs (Fig. 14g-i), while both the sedimentation rate and the advance velocity of the

440 position of maximum deposition increase during the final period of deposition (Fig. 14d-i).

441

442 **4. Discussion**

443 In this work we have presented a new model to describe dam-break fluidized granular flows

444 and test the effect of low-angle inclined surfaces in the resulting propagation dynamics. This

445 model, built on the formulation described by Chupin et al. (2021) for dry flows, was compared

446 with a benchmark analogue experiment for which detailed information of flow propagation,

447 pore pressure evolution and sedimentation dynamics is available in the literature (Roche et al.

448 2010; Roche 2012). Thereby, this work complements previous efforts to analyse analogue

449 experiments through numerical modeling (Breard et al. 2019a). In particular, Breard et al.

450 (2019a) tested different friction models and compared their simulations with experiments

451 considering flow shape, kinematics and pore pressure evolution. Our model allows the

452 description of the sedimentation dynamics of granular flows and their comparison with

453 additional characteristics of the benchmark experiment (Roche et al. 2010; Roche 2012), thus

454 allowing to explore aspects of granular flows that were not addressed by Breard et al. (2019a).

455 In contrast, the model of Breard et al. (2019a) is able to describe slight compaction and dilation

456 processes, which is not possible in our formulation.

457 Numerical results reproduce reasonably well the collapse and propagation dynamics described

458 in the analogue experiment in terms of run-out distance and pore pressure, and they allow to

459 constrain the effective diffusion coefficient that characterizes the granular material considered.

460 However, even though the model captures the general shape of the resulting deposits, the

461 thickness tends to be under-estimated in proximal domains and over-estimated in distal

462 domains. Potential sources of systematic differences between analogue experiments and our

463 numerical model are the dynamics of gate opening and simplifications in the mathematical

464 description such as the non-compressibility of the granular flow and the assumption of a

465 constant effective diffusion coefficient in space and time.

466 Interestingly, our estimates of the effective diffusion coefficient are consistent with

467 experimental measurements on static defluidizing beds (Roche et al. 2010) and are one order

468 of magnitude smaller than the theoretical value, which fails completely in predicting the

469 behaviour of the studied analogue experiment (see Fig. 1d). The discrepancy between the

470 theoretical value and experiment-derived estimates (Roche et al. 2010; Montserrat et al. 2012)

471 is a major unsolved issue related to pore pressure diffusion in granular materials. Breard et al.

472 (2019b) showed that if the volume of air in a windbox at the base of an experimental granular

473 column is significant compared to the volume of air in the column, then the measured diffusion

474 coefficient is larger than predicted theoretically. However, we made recently further pore

475 pressure diffusion tests in a device with a windbox whose volume was less than ~0.05 % of the

476 volume of air in the granular column, and we found a positive correlation between the diffusion

477 coefficient and the column height (in preparation). Therefore, though a windbox affects the

478 estimates of pore pressure diffusion coefficient, it cannot be invoked to explain differences of

479 more than one order of magnitude between experimental and theoretical estimates, and thus

480 additional investigation is still required to understand this discrepancy. In the case of the

481 numerical simulations presented here, we note that the effective diffusion coefficients $\kappa =$

482 $0.015 - 0.035 \text{ m}^2/\text{s}$ giving the best agreement with the experimental data are those typical of

483 static bed heights of ~15–25 cm, which are about half the height of the initial column in the

484 dam-break configuration. This typical height seems to be the best compromise between the

485 height of the column released and that of the resulting flow.

486 Despite that main differences in flow dynamics due to different diffusion coefficients arise

487 during only the first ~17-22% of the total propagation time, they can cause significant changes

488 in the resulting run-out distance. In contrast, during the later phases of flow propagation, once

489 pore pressure has diffused significantly, the non-fluidized conditions of the flow produce a

490 similar stopping dynamics in all the simulations studied. These results suggest that

491 understanding the processes controlling the generation and evolution of pore pressure (e.g.

492 internal gas-particle motion, air ingestion, particle settling and diffusion; Sweeney and

493 Valentine 2017; Valentine and Sweeney 2018; Valentine 2020; Fries et al. 2021) at early

494 propagation stages can be particularly critical in controlling the whole granular flow, regardless

495 of possible mechanisms able to generate pore pressure during later propagation stages (Benage

496 et al. 2016; Breard et al. 2018; Chédeville and Roche 2015, 2018; Lube et al. 2019), which are

497 not taken into account in our numerical model and are expected to be negligible in the

498 benchmark experiment. In simulations on horizontal surfaces with effective diffusion

499 coefficients compatible with the benchmark experiment, we observe an increase of run-out

500 distance by a factor of ~1.8–2.2 when compared with dry granular flows. Thus, fluidization

501 processes represent a critical factor in the evaluation of PDC hazard.

502 Additionally, this work provides insights for understanding some aspects of the dynamics of

503 fluidized granular flows such as the evolution of pore pressure in time and space, the deposition

504 process, and the effect of inclined topographies. These aspects are discussed below:

505   a) Our simulations of initially fluidized flows present an initial phase dominated by pore

506   pressure advection and a later phase controlled by pore pressure diffusion up to reach

507   stationary conditions. The transition between these phases is influenced by the effect of

508   front velocity on flow stretching because pore pressure diffuses faster in thinner flows.

509   Importantly, these results suggest that the fluidization effect in increasing the maximum

510   run-out distance may be self-limited, particularly on steep slopes. In fact, high pore

511   pressure reduces friction and causes faster granular flows able to travel larger distances,

512   but in turn fast propagation causes reduction in flow thickness, which causes faster pore

513   pressure diffusion.

514 b) The basal pore pressure simulated at a given point along the channel shows an over-

515   pressure phase coincident with the passage of the flow head, while the pressure signal

516   measured in experiments beneath the flow substrate interface, which represents the

517   difference between the pressure at the flow base and the ambient atmospheric pressure,

518   is characterized by a short under-pressure phase followed by a longer over-pressure

519   stage. Although comparing these data is not straightforward because the experimental

520   data are partially influenced by processes not considered in our model, in this work we

521   analyzed the main characteristics of these signals and we also considered the influence

522   of the basal slip conditions, as suggested in the literature (Roche et al. 2010; Breard et

523   al. 2019a). We show that the relationship between distance along the channel and the

524   maximum pressure reached during the flow passage is remarkably similar in simulations

525   and experiments, which indicates that our model is able to capture reasonably well the

526   evolution of pore pressure within the granular flow. This suggests that the effect of

527   compaction and dilatancy processes (Bouchut et al. 2016, 2021) is limited once the flow

528   front has passed, and that the pore pressure effect in the propagation of granular flows

529   can be modeled considering only advection. Moreover, we show that the magnitude of

530   the under-pressure phase measured in experiments can be successfully quantified by

531   considering the slip velocity at the channel base, as proposed by Breard et al. (2019a).

532 c) Our simulations suggest that deposition is close to the *en masse* end-member. In fact,

533   for a given point along the channel, the time-span during which deposition occurs is

534   much smaller than the timescale of granular flow propagation. Our results show that the

535   position at which the maximum of sedimentation rate occurs advances monotonically

536   from the reservoir and it is strongly influenced by the surface slope angle, while the

537   effect of the pore pressure diffusion coefficient is small. Our conclusion on deposition

538   is relevant for the experimental configuration considered but it is not necessarily

539   applicable for natural systems of significantly larger scale. In nature, in fact, progressive

540   aggradation can operate if onset of deposition occurs at early stages, the flow thickness

541   is large and the deposition rate is low (see Fig. 12 of Roche 2012).

542   d) Numerical simulations on inclined surfaces have shown that a low slope angle (up to

543   10°) is able to increase the run-out distance by a factor of 2.05 – 2.25 when compared

544   with horizontal surfaces. This has major implications for pyroclastic density currents,

545   which typically propagate at gentle slope angles. A remarkable example where the

546   regional slope could exert a significant effect is the Cerro Galan Ignimbrite (NW

547   Argentina; Francis et al. 1983; Cas et al. 2011; Lesti et al. 2011), which presents a

548   maximum run-out distance of ~70 km and was emplaced on a regional regular slope of

549   a few degrees. Cas et al. (2011) also suggested an important effect of gas pore pressure

550   in the reduction of friction between the flow and the substrate in this case study. Another

551   example is the Peach Spring Tuff (USA), formed by PDCs that travelled >170 km from

552   the eruptive centre and propagated on substrates with gentle slope angles (Valentine et

553   al. 1989; Roche et al. 2016). In this case as well, a significant influence of gas pore

554   pressure in the resulting run-out distance has been suggested (Roche et al. 2016). Notice

555   that though regional slope may enhance the runout distance of PDCs, recent advances

556   suggest that the latter is controlled fundamentally by the discharge rate (Roche et al.

557   2021).

558

5. Concluding remarks

The numerical simulations presented in this work and their comparison with published experimental data have revealed that:

(1) Even though the pore pressure diffusion coefficient probably varies in space and time in dam-break fluidized granular flows, a constant (effective) pore pressure diffusion coefficient can be estimated to capture reasonably well the flow dynamics in terms of run-out distance, temporal evolution of pore fluid pressure, and shape of the deposit.

(2) Pore pressure increases significantly the run-out distance of initially fluidized granular flows when compared with dry granular flows (e.g., by a factor of ~1.8 – ~2.2 on horizontal slopes). Therefore, taking into account pore fluid pressure appears critical for modelling dense PDCs in the context of volcanic hazard assessment.

(3) A significant effect in granular flow run-out is also exerted by the substrate slope angle. For given fluidization conditions, an increase of slope angle from 0° to 10° produces an increment of the run-out distance of 105 – 125%.

(4) The effect of fluidization in increasing run-out distance may be self-limited because the higher velocity due to fluidization tends to reduce flow thickness, which induces faster pore pressure diffusion.

(5) The pore pressure evolution in initially fluidized granular flows is mainly controlled by the diffusion coefficient, while the effect of the angle slope of the substrate is limited.

(6) In the dam-break configuration at laboratory scale, the onset of the deposition of granular flows occurs with a significant delay with respect to the front propagation. Once deposition starts, the position at which the maximum sedimentation rate occurs advances monotonically with time at a velocity significantly larger than the flow front velocity. The dynamics of sedimentation in the studied experimental configuration, which is a direct consequence of the rheological model adopted and does not require

584   calibrated inputs to set the sedimentation rate, is close to the *en masse* end-member

585   model, but more progressive aggradation may operate in nature.

586   (7) Our model describes depth-dependent variations of the properties of granular flows

587   considering high-aspect ratio dam-break configurations. Moreover, the possibility of

588   exploring granular flows at larger length-scale makes this model a promising tool for

589   investigating the factors controlling the dynamics of long run-out PDCs in nature.

590

599

600 **References**

601 Balay S, Abhyankar S, Adams M, Brown J, Brune P, Buschelman K, Dalcin L, Dener A,

602   Eijkhout V, Gropp W, Karpeyev D, Kaushik D, Knepley M, May D, McInnes LC, Mills

603   R, Munson T, Rupp K, Sanan P, Smith B, Zampini S, Zhang H (2018a) PETSc Users

604   Manual Revision 3.10 (Technical Report ANL-95/11 - Revision 3.10). Argonne

605   National Laboratory (ANL), Argonne, IL (United States).

606 Balay S, Abhyankar S, Adams M, Brown J, Brune P, Buschelman K, Dalcin L, Dener A,

607   Eijkhout V, Gropp W, Kaushik D, Knepley M, May D, McInnes LC, Mills R, Munson

608   T, Rupp K, Sanan P, Smith B, Zampini S, Zhang H (2018b) PETSc Web page. http://www.mcs.anl.gov/petsc

609   http://www.mcs.anl.gov/petsc

610   Benage M, Dufek J, Mothes P (2016) Quantifying entrainment in pyroclastic density currents

611   from the Tungurahua eruption, Ecuador: Integrating field proxies with numerical

612   simulations. Geophysical Research Letters 43(13):6932-6941.

613   https://doi.org/10.1002/2016GL069527

614   Bernard J, Kelfoun K, Le Pennec J, Vallejo Vargas S (2014) Pyroclastic flow erosion and

615   bulking processes: comparing field-based vs modeling results at Tungurahua volcano,

616   Ecuador. Bulletin of Volcanology 76(9):1-16.

617   https://doi.org/10.1007/s00445-014-0858-y

618   Bouchut F, Fernández-Nieto E, Mangeney A, Narbona-Reina G (2016) A two-phase two-layer

619   model for fluidized granular flows with dilatancy effects. Journal of Fluid Mechanics

620   801:166-221. https://doi.org/10.1017/jfm.2016.417

621   Bouchut F, Fernández-Nieto E, Mangeney A, Narbona-Reina G (2021) Dilatancy in dry

622   granular flows with a compressible $\mu(I)$ rheology. Journal of Computational Physics

623   429:110013. https://doi.org/10.1016/j.jcp.2020.110013

624   Brand B, Mackaman-Lofland C, Pollock N, Bendaña S, Dawson B, Wichgers P (2014)

625   Dynamics of pyroclastic density currents: Conditions that promote substrate erosion and

626   self-channelization—Mount St Helens, Washington (USA). Journal of Volcanology and

627   Geothermal Research 276:189-214. https://doi.org/10.1016/j.jvolgeores.2014.01.007

628   Branney M, Kokelaar P (2002) Pyroclastic density currents and the sedimentation of

629   ignimbrites. Geological Society of London.

630   Breard EC, Lube G, Jones JR, Dufek J, Cronin SJ, Valentine GA, Moebis A (2016) Coupling

631   of turbulent and non-turbulent flow regimes within pyroclastic density currents. Nature

632   Geoscience 9(10):767-771. https://doi.org/10.1038/ngeo2794

633 Breard E, Dufek J, Lube G (2018) Enhanced mobility in concentrated pyroclastic density

634   currents: An examination of a self-fluidization mechanism. Geophysical Research

635   Letters, 45(2), 654-664. https://doi.org/10.1002/2017GL075759

636 Breard EC, Dufek J, Roche O (2019a) Continuum modeling of pressure-balanced and fluidized

637   granular flows in 2-D: Comparison with glass bead experiments and implications for

638   concentrated pyroclastic density currents. Journal of Geophysical Research: Solid Earth

639   124(6):5557-5583. https://doi.org/10.1029/2018JB016874

640 Breard EC, Jones, JR, Fullard L, Lube G, Davies C, Dufek J (2019b) The permeability of

641   volcanic mixtures—implications for pyroclastic currents. Journal of Geophysical

642   Research: Solid Earth 124(2):1343-1360. https://doi.org/10.1029/2018JB016544

643 Burgisser A (2012) A semi-empirical method to calculate the permeability of homogeneously

644   fluidized pyroclastic material. Journal of Volcanology and Geothermal Research 243:

645   97-106. https://doi.org/10.1016/j.jvolgeores.2012.08.015

646 Burgisser A, Bergantz G (2002) Reconciling pyroclastic flow and surge: the multiphase physics

647   of pyroclastic density currents. Earth and Planetary Science Letters 202(2):405-418.

648   https://doi.org/10.1016/S0012-821X(02)00789-6

649 Bursik MI, Woods AW (1996) The dynamics and thermodynamics of large ash-flows. Bulletin

650   of Volcanology 58:175-93. https://doi.org/10.1007/s004450050134

651 Cas R, Wright H, Folkes C, Lesti C, Porreca M, Giordano G, Viramonte J (2011) The flow

652   dynamics of an extremely large volume pyroclastic flow, the 2.08-Ma Cerro Galán

653   Ignimbrite, NW Argentina, and comparison with other flow types. Bulletin of

654   Volcanology 73(10):1583-1609. https://doi.org/10.1007/s00445-011-0564-y

655 Chalayer R, Chupin L, Dubois T (2018) A bi-projection method for incompressible bingham

656   flows with variable density, viscosity, and yield stress. SIAM Journal on Numerical

657   Analysis 56(4):2461-2483. https://doi.org/10.1137/17M113993X

658   Chédeville C, Roche O (2015) Influence of slope angle on pore pressure generation and

659   kinematics of pyroclastic flows: insights from laboratory experiments. Bulletin of

660   Volcanology 77(11):1-13. https://doi.org/10.1007/s00445-015-0981-4

661   Chédeville C, Roche O (2018) Autofluidization of collapsing bed of fine particles: implications

662   for the emplacement of pyroclastic flows. Journal of Volcanology and Geothermal

663   Research 368:91-99. https://doi.org/10.1016/j.jvolgeores.2018.11.007

664   Chupin L, Dubois T (2016) A bi-projection method for Bingham type flows. Computers &

665   Mathematics with Applications 72(5):1263-1286.

666   https://doi.org/10.1016/j.camwa.2016.06.026

667   Chupin L, Dubois T, Phan M, Roche O (2021) Pressure-dependent threshold in a granular flow:

668   Numerical modeling and experimental validation. Journal of Non-Newtonian Fluid

669   Mechanics 291:104529. https://doi.org/10.1016/j.jnnfm.2021.104529

670   Cole P, Neri A, Baxter P (2015) Hazards from pyroclastic density currents. In: The

671   Encyclopedia of Volcanoes (pp. 943-956). Academic Press.

672   Druitt T (1998) Pyroclastic density currents. Geological Society, London, Special Publications

673   145(1):145-182.

674   Druitt T, Avard G, Bruni G, Lettieri P, Maez F (2007) Gas retention in fine-grained pyroclastic

675   flow materials at high temperatures. Bulletin of Volcanology 69(8):881-901.

676   https://doi.org/10.1007/s00445-007-0116-7

677   Dufek J (2016) The fluid mechanics of pyroclastic density currents. Annual Review of Fluid

678   Mechanics 48:459-485. https://doi.org/10.1146/annurev-fluid-122414-034252

679   Dufek J, Esposti Ongaro T, Roche O (2015) Pyroclastic density currents: processes and models.

680   In: The Encyclopedia of Volcanoes (pp. 617-629). Academic Press.

681   Esposti Ongaro T, Cerminara M, Charbonnier S, Lube G, Valentine G (2020) A framework for

682   validation and benchmarking of pyroclastic current models. Bulletin of Volcanology

683   82:1-17. https://doi.org/10.1007/s00445-020-01388-2

684   Farin M, Mangeney A, Roche O (2014) Fundamental changes of granular flow dynamics,

685   deposition, and erosion processes at high slope angles: insights from laboratory

686   experiments. Journal of Geophysical Research: Earth Surface 119(3):504-532.

687   https://doi.org/10.1002/2013JF002750

688   Francis P, O'Callaghan L, Kretzschmar G, Thorpe R, Sparks R, Page R, De Barrio R, Gillou G,

689   Gonzalez O (1983) The Cerro Galan ignimbrite. Nature 301(5895):51-53.

690   https://doi.org/10.1038/301051a0

691   Fries A, Roche O, Carazzo G (2021) Granular mixture deflation and generation of pore fluid

692   pressure at the impact zone of a pyroclastic fountain: Experimental insights. Journal of

693   Volcanology and Geothermal Research 414:107226.

694   https://doi.org/10.1016/j.jvolgeores.2021.107226

695   Fullmer WD, Hrenya CM (2017) The clustering instability in rapid granular and gas-solid

696   flows. Annual Review of Fluid Mechanics 49:485-510.

697   https://doi.org/10.1146/annurev-fluid-010816-060028

698   Garres-Díaz J, Bouchut F, Fernández-Nieto E, Mangeney A, Narbona-Reina G (2020)

699   Multilayer models for shallow two-phase debris flows with dilatancy effects. Journal of

700   Computational Physics 419:109699. https://doi.org/10.1016/j.jcp.2020.109699

701   Gase A, Brand B, Bradford J (2017) Evidence of erosional self-channelization of pyroclastic

702   density currents revealed by ground-penetrating radar imaging at Mount St. Helens,

703   Washington (USA). Geophysical Research Letters 44(5):2220-2228.

704   https://doi.org/10.1002/2016GL072178

705   Giordano G, Cas RAF (2021) Classification of ignimbrites and their eruptions. Earth-Science

706   Reviews 220:103697. https://doi.org/10.1016/j.earscirev.2021.103697

707   Goren L, Aharonov E, Sparks D, Toussaint R (2010) Pore pressure evolution in deforming

708   granular material: A general formulation and the infinitely stiff approximation. Journal

709   of Geophysical Research: Solid Earth 115(B9). https://doi.org/10.1029/2009JB007191

710   Gray J, Edwards A (2014) A depth-averaged μ(I)-rheology for shallow granular free-surface

711   flows. Journal of Fluid Mechanics 755:503-534. https://doi.org/10.1017/jfm.2014.450

712   Gueugneau V, Kelfoun K, Roche O, Chupin L (2017) Effects of pore pressure in pyroclastic

713   flows: numerical simulation and experimental validation. Geophysical Research Letters

714   44(5):2194-2202. https://doi.org/10.1002/2017GL072591

715   Ionescu I, Mangeney A, Bouchut F, Roche O (2015) Viscoplastic modeling of granular column

716   collapse with pressure-dependent rheology. Journal of Non-Newtonian Fluid Mechanics

717   219:1-18. https://doi.org/10.1016/j.jnnfm.2015.02.006

718   Iverson R (1997) The physics of debris flows. Reviews of Geophysics 35(3):245-296.

719   https://doi.org/10.1029/97RG00426

720   Iverson R, Denlinger R (2001) Flow of variably fluidized granular masses across three-

721   dimensional terrain: 1. Coulomb mixture theory. Journal of Geophysical Research:

722   Solid Earth 106(B1):537-552. https://doi.org/10.1029/2000JB900329

723   Jop P, Forterre Y, Pouliquen O (2006) A constitutive law for dense granular flows. Nature

724   441(7094):727-730. https://doi.org/10.1038/nature04801

725   Kelfoun K (2011) Suitability of simple rheological laws for the numerical simulation of dense

726   pyroclastic flows and long-runout volcanic avalanches. Journal of Geophysical

727   Research: Solid Earth 116(B8). https://doi.org/10.1029/2010JB007622

728   Lesti C, Porreca M, Giordano G, Mattei M, Cas R, Wright H, Folkes C, Viramonte J (2011)

729   High-temperature emplacement of the Cerro Galán and Toconquis Group ignimbrites

730   (Puna plateau, NW Argentina) determined by TRM analyses. Bulletin of Volcanology

731   73(10):1535-1565. https://doi.org/10.1007/s00445-011-0536-2

732   Lube G, Breard EC, Jones J, Fullard L, Dufek J, Cronin SJ, Wang T (2019) Generation of air

733   lubrication within pyroclastic density currents. Nature Geoscience 12(5):381-386.

734   https://doi.org/10.1038/s41561-019-0338-2

735   Lube G, Breard EC, Esposti Ongaro T, Dufek J, Brand B (2020) Multiphase flow behaviour

736   and hazard prediction of pyroclastic density currents. Nature Reviews Earth &

737   Environment 1(7):348-365. https://doi.org/10.1038/s43017-020-0064-8

738   Marino B, Thomas L, Linden P (2005) The front condition for gravity currents. Journal of Fluid

739   Mechanics 536:49-78. https://doi.org/10.1017/S0022112005004933

740   Montserrat S, Tamburrino A, Roche O, Niño Y (2012) Pore fluid pressure diffusion in

741   defluidizing granular columns. Journal of Geophysical Research: Earth Surface

742   117(F2). https://doi.org/10.1029/2011JF002164

743   Neri A, Esposti Ongaro T, Voight B, Widiwijayanti C (2015) Pyroclastic density current

744   hazards and risk. In: Volcanic Hazards, Risks and Disasters (pp. 109-140). Elsevier.

745   Osher S, Fedkiw R (2001) Level set methods: an overview and some recent results. Journal of

746   Computational Physics 169(2):463-502. https://doi.org/10.1006/jcph.2000.6636

747   Roche O (2012) Depositional processes and gas pore pressure in pyroclastic flows: an

748   experimental perspective. Bulletin of Volcanology 74(8):1807-1820.

749   https://doi.org/10.1007/s00445-012-0639-4

750   Roche O, Montserrat S, Niño Y, Tamburrino A (2010) Pore fluid pressure and internal

751   kinematics of gravitational laboratory air-particle flows: Insights into the emplacement

752   dynamics of pyroclastic flows. Journal of Geophysical Research: Solid Earth 115(B9).

753   https://doi.org/10.1029/2009JB007133

754   Roche O, Buesch D, Valentine G (2016) Slow-moving and far-travelled dense pyroclastic flows

755   during the Peach Spring super-eruption. Nature Communications 7(1):1-8.

756   https://doi.org/10.1038/ncomms10890

757   Roche O, Azzaoui N, Guillin A (2021) Discharge rate of explosive volcanic eruption controls

758   runout distance of pyroclastic density currents. Earth and Planetary Science Letters

759   568:117017. https://doi.org/10.1016/j.epsl.2021.117017

760   Rowley P, Roche O, Druitt T, Cas R (2014) Experimental study of dense pyroclastic density

761   currents using sustained, gas-fluidized granular flows. Bulletin of Volcanology 76(9):1-

762   13. https://doi.org/10.1007/s00445-014-0855-1

763   Savage S, Iverson R (2003) Surge dynamics coupled to pore-pressure evolution in debris flows.

764   In : Proc. 3rd Int. Conf. on Debris-Flow Hazards Mitigation: Mechanics, Prediction, and

765   Assessment. Edited by: Rickenmann D, Chen CL. Millpress, Rotterdam (pp. 503-514).

766   Shimizu H, Koyaguchi T, Suzuki Y (2019) The run-out distance of large-scale pyroclastic

767   density currents: a two-layer depth-averaged model. Journal of Volcanology and

768   Geothermal Research 381:168-184. https://doi.org/10.1016/j.jvolgeores.2019.03.013

769   Smagorinsky J (1963) General circulation experiments with the primitive equations: I. The

770   basic experiment. Monthly Weather Review 91(3):99-164.

771   Sweeney M, Valentine G (2017) Impact zone dynamics of dilute mono-and polydisperse jets

772   and their implications for the initial conditions of pyroclastic density currents. Physics

773   of Fluids 29(9):093304. https://doi.org/10.1063/1.5004197

774   Valentine G (2019) Preface to the topical collection—pyroclastic current models:

775   benchmarking   and   validation.   Bulletin   of   Volcanology   81:69.

776   https://doi.org/10.1007/s00445-019-1328-3

777   Valentine G (2020) Initiation of dilute and concentrated pyroclastic currents from collapsing

778   mixtures and origin of their proximal deposits. Bulletin of Volcanology 82(2):1-24.

779   https://doi.org/10.1007/s00445-020-1366-x

780   Valentine G, Buesch D, Fisher R (1989) Basal layered deposits of the Peach Springs Tuff,

781   northwestern Arizona, USA. Bulletin of Volcanology 51(6):395-414.

782   https://doi.org/10.1007/BF01078808

783   Valentine G, Doronzo D, Dellino P, de Tullio M (2011) Effects of volcano profile on dilute

784   pyroclastic density currents: numerical simulations. Geology 39(10):947-950.

785   https://doi.org/10.1130/G31936.1

786   Valentine G, Sweeney M (2018) Compressible flow phenomena at inception of lateral density

787   currents fed by collapsing gas-particle mixtures. Journal of Geophysical Research: Solid

788   Earth 123(2):1286-1302. https://doi.org/10.1002/2017JB015129

789   Wilson C (1984) The role of fluidization in the emplacement of pyroclastic flows, 2:

790   experimental results and their interpretation. Journal of Volcanology and Geothermal

791   Research 20(1-2):55-84. https://doi.org/10.1016/0377-0273(84)90066-0

792
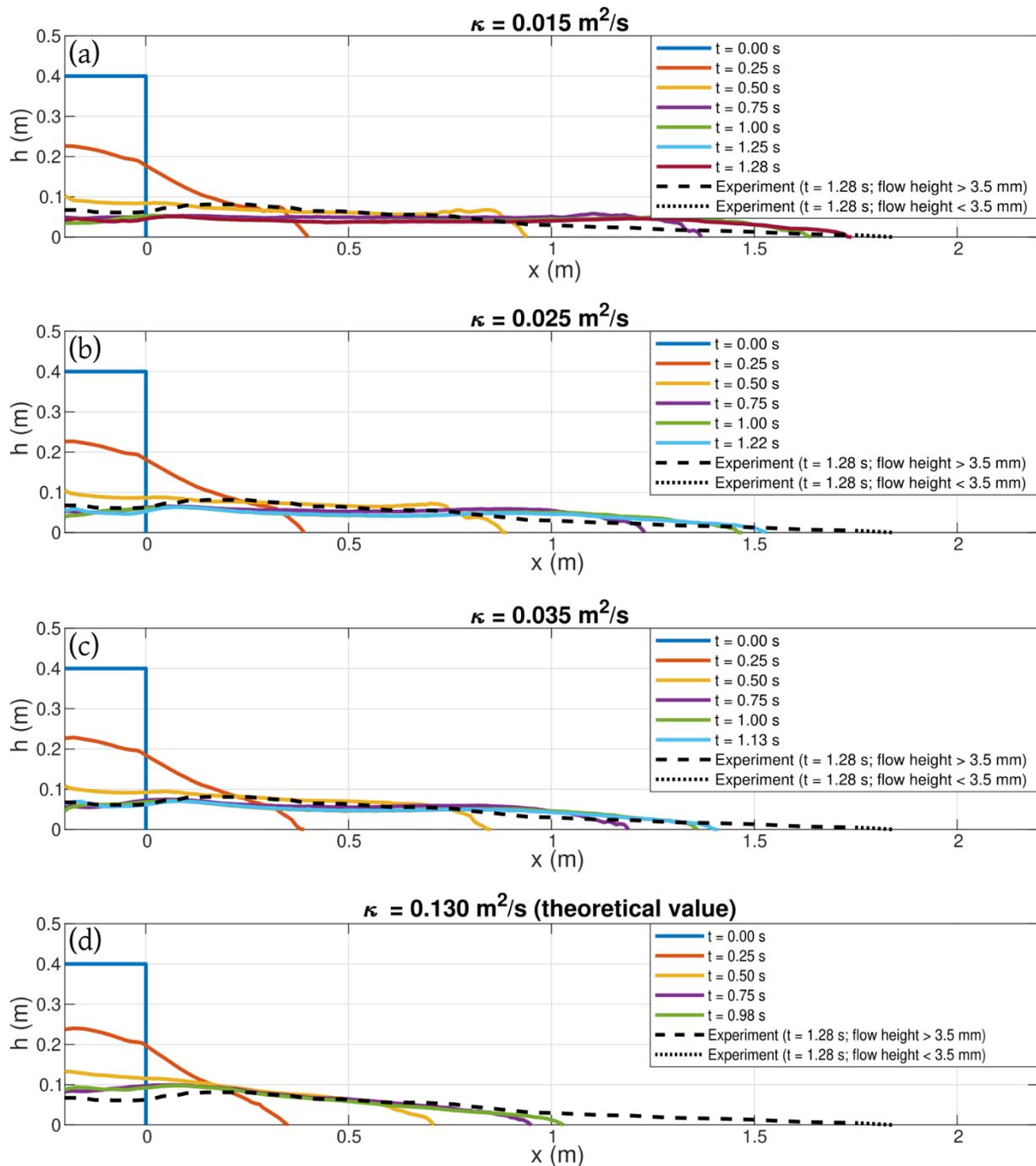
Figures

Figure 1. Surface profiles of the granular flows at different times after release (see legends) in four simulations performed on horizontal planes, considering initially fluidized conditions and different values of the effective diffusion coefficient (κ, see titles). The final surface profile of the benchmark analogue experiment is also included (Roche et al. 2010).
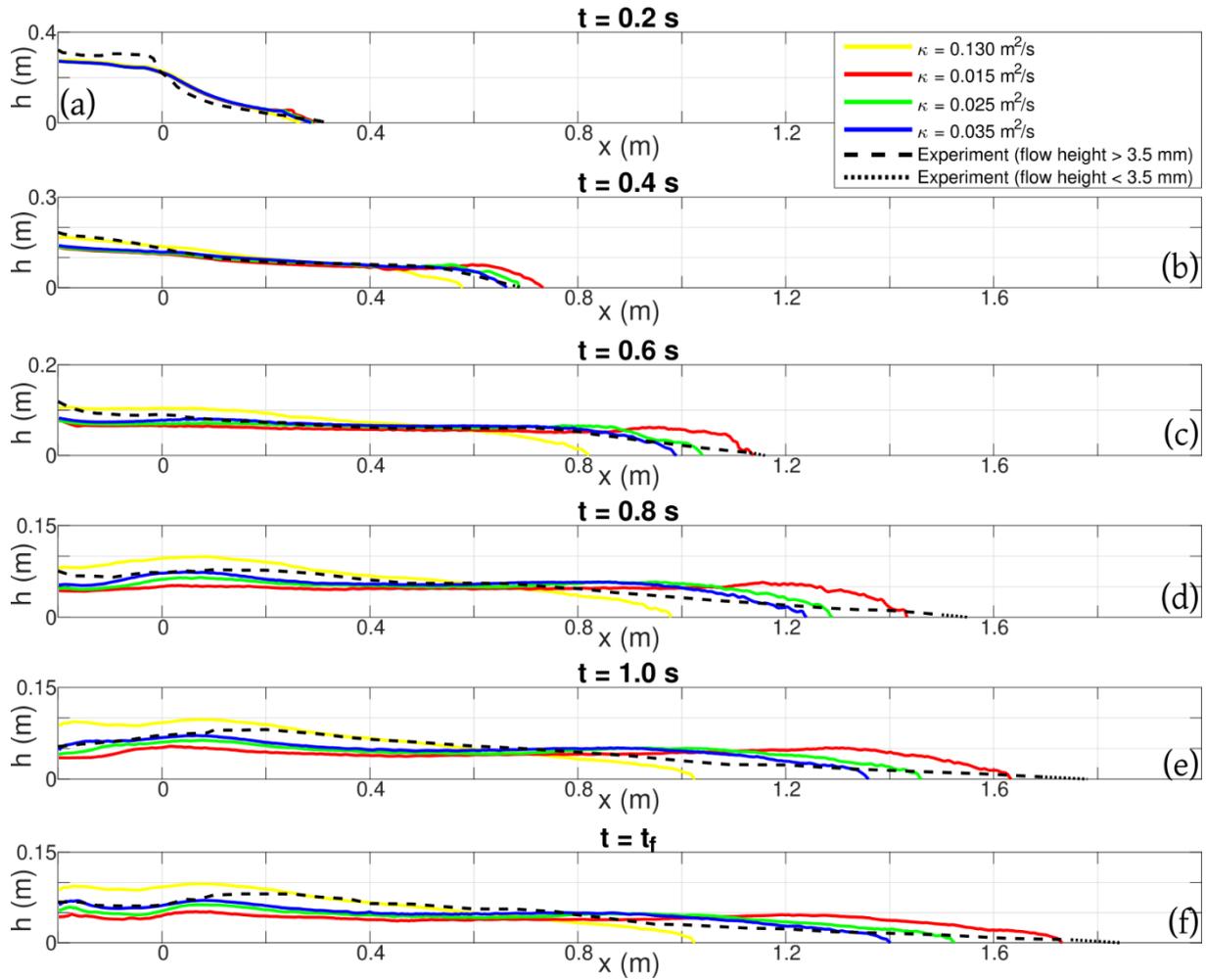
Figure 2. Surface profiles of the granular flows at different times after release in four simulations performed on horizontal planes, considering initially fluidized conditions and different values of the effective diffusion coefficient (κ, see legend). The evolution of the surface profile of the benchmark analogue experiment is also included (Roche et al. 2010).

807
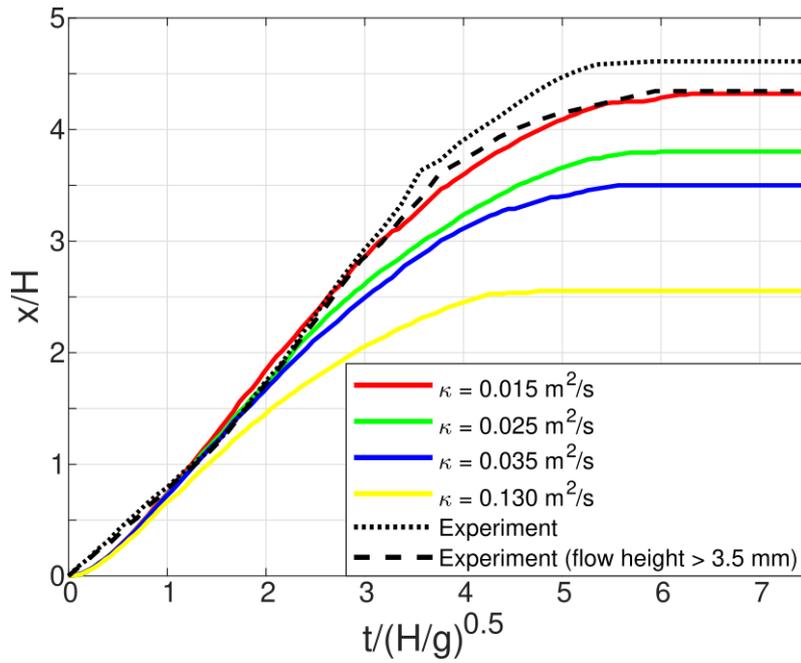
Figure 3. Temporal evolution of the front position of the granular flows in four simulations

performed on horizontal planes, considering initially fluidized conditions and different values

of the effective diffusion coefficient (κ, see legend). The temporal evolution of the front

position of the benchmark analogue experiment is shown as well (see legend; Roche et al.

2010). Because our simulations are not able to describe flow thicknesses lower than 3.5 mm

(i.e. the cell size used in numerical simulations), we also include the experimental data

considering only flow thicknesses above this threshold in the definition of the front position.

Both axes are normalized using ad-hoc factors in order to produce non-dimensional results

($H = 0.4$ m and $g = 9.8$ m/s^2).

819
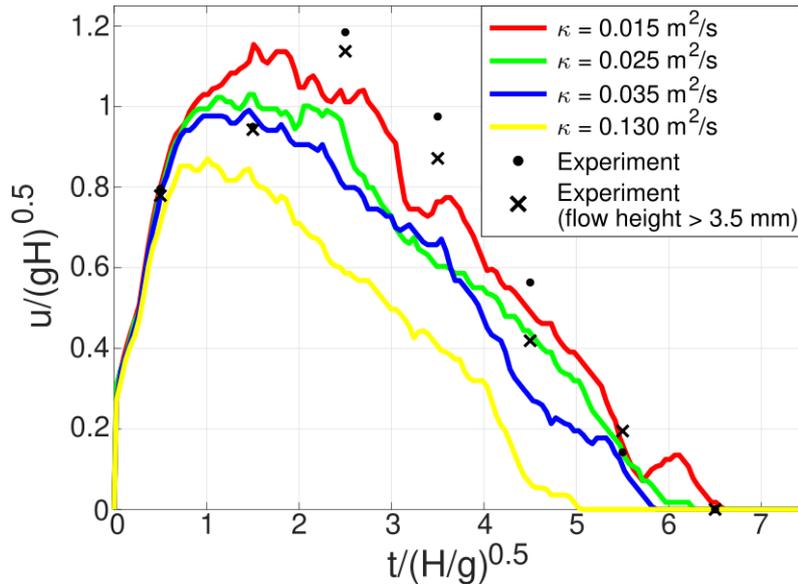
Figure 4. Temporal evolution of the front velocity of the granular flows in four simulations performed on horizontal planes, considering initially fluidized conditions and different values of the effective diffusion coefficient (κ, see legend). A moving average function was applied to these curves, considering a time window of 0.1 s. The evolution of the front velocity of the benchmark analogue experiment is shown as well (see legend; Roche et al. 2010). Because our simulations are not able to describe flow thicknesses lower than 3.5 mm (i.e. the cell size used in numerical simulations), we include the experimental data considering only flow thicknesses above this threshold in the definition of the front position. Both axes are normalized using ad-hoc factors in order to produce non-dimensional results ($H = 0.4$ m and $g = 9.8$ m/s^2). Note that the theoretical value for the maximum velocity in a dam-break experiment of an inviscid flow is $u/\sqrt{gH} = \sqrt{2} \approx 1.4$ (Marino et al. 2005).

831

832
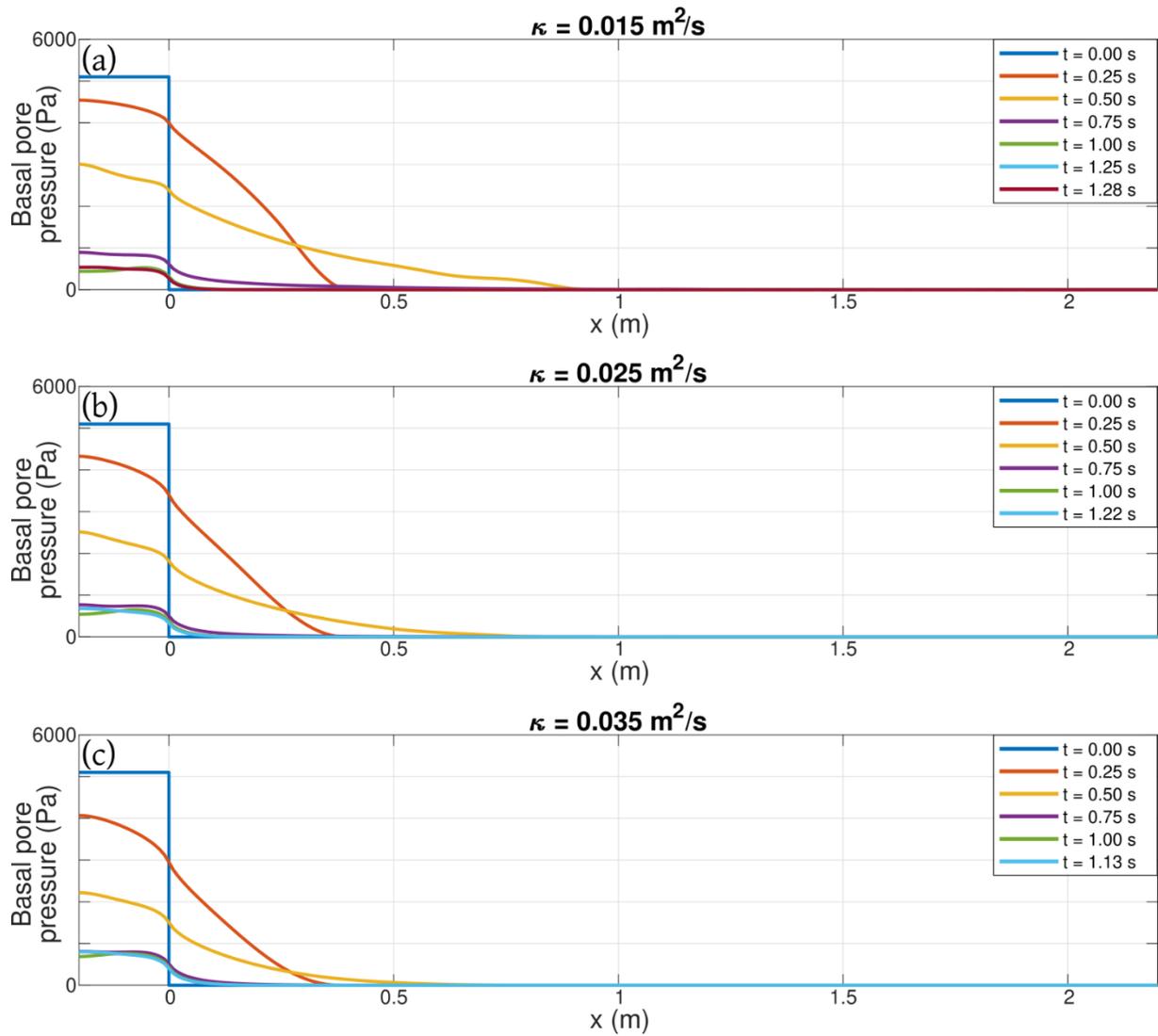
Figure 5. Basal pore pressure profiles of the granular flows at different times after release (see legends) in three simulations performed on horizontal planes, considering initially fluidized conditions and different values of the effective diffusion coefficient (κ, see titles). Note that the ratio between basal pore pressure and the lithostatic pressure ($p_f/\rho gh$), not shown here, represents the degree of fluidization (see Supplementary Figure S1). Full fluidization occurs when $p_f/\rho gh$ is larger than one.
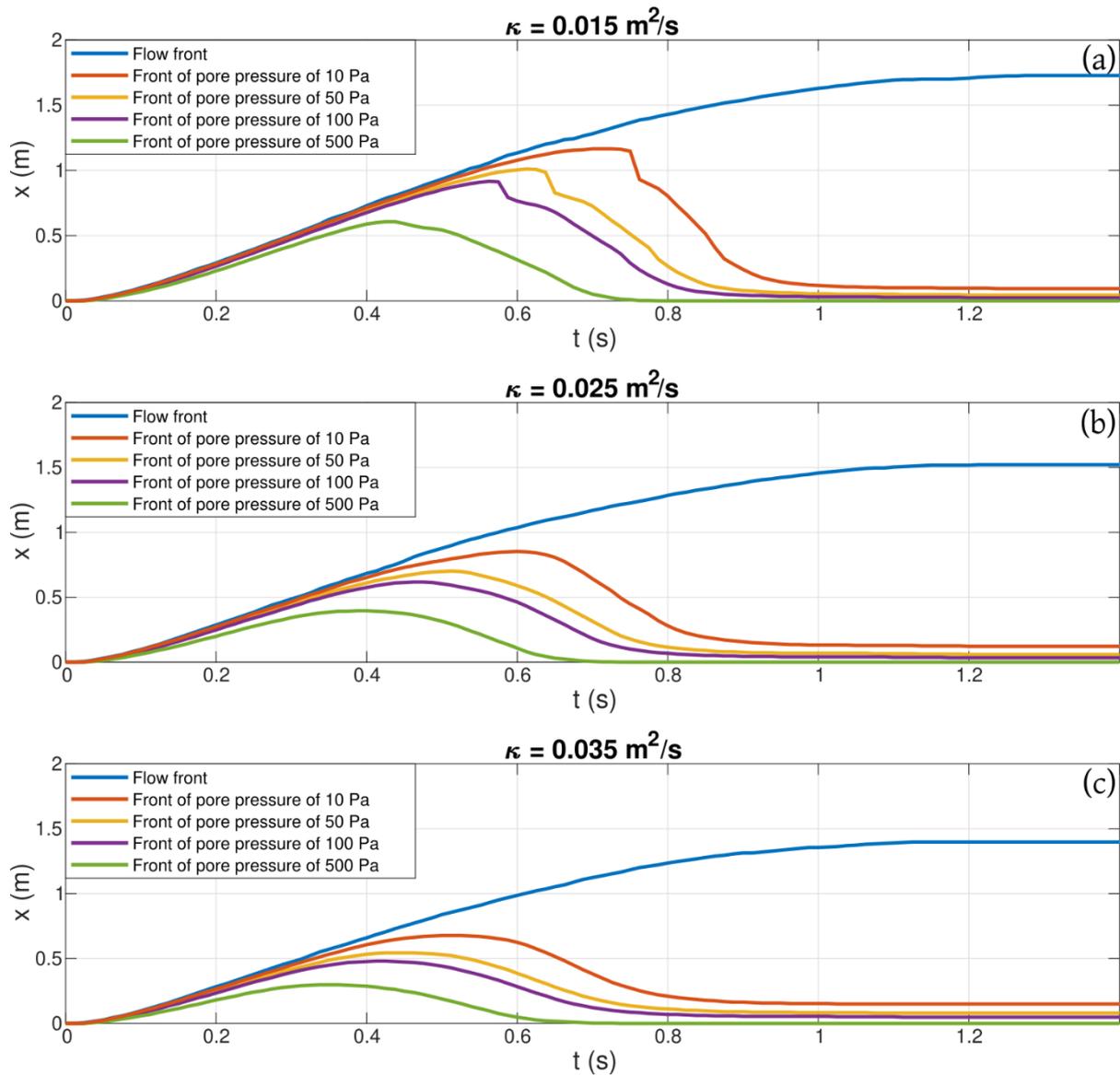
Figure 6. Temporal evolution of the front position and a set of iso-pressure fronts (i.e. the position along the x-axis at which specific values of pore pressure are reached as a function of time, see legends) in three simulations performed on horizontal planes, considering initially fluidized conditions and different values of the effective diffusion coefficient (κ, see titles).

849
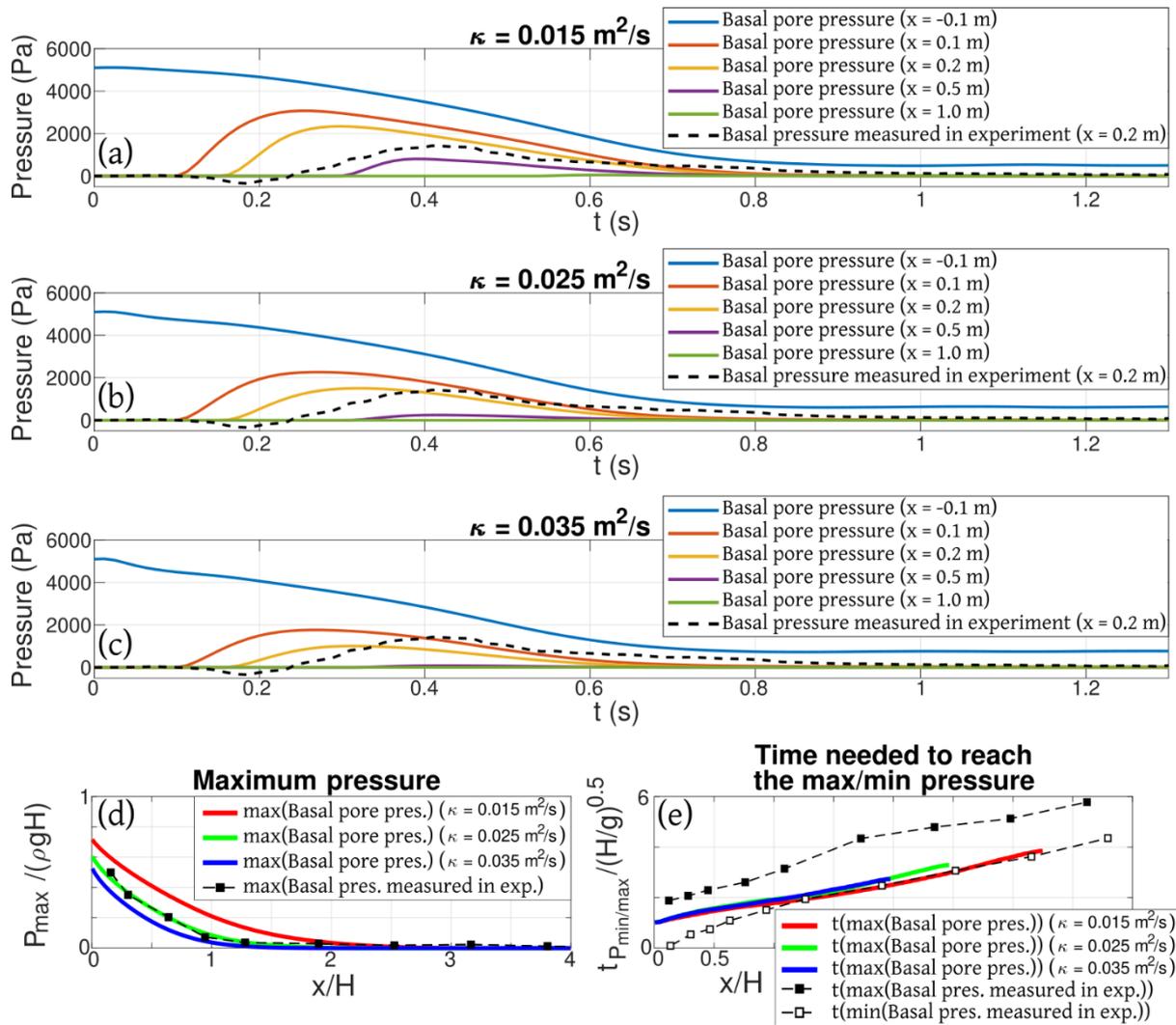
Figure 7. (a-c) Temporal evolution of basal pore pressure at different positions (see legends) in simulations on horizontal planes, considering initially fluidized conditions and different values of the effective diffusion coefficient (κ, see titles). Experimental data are also presented (Roche et al. 2010). (d) Maximum normalized values of basal pressure in numerical simulations and in the benchmark experiment as a function of horizontal distance (see legend; Roche et al. 2010). (e) Time needed to reach the extreme values of basal pressure (i.e. minimum, if present, and maximum values) at the channel base in numerical simulations and in the benchmark experiment (see legend; Roche et al. 2010).

858
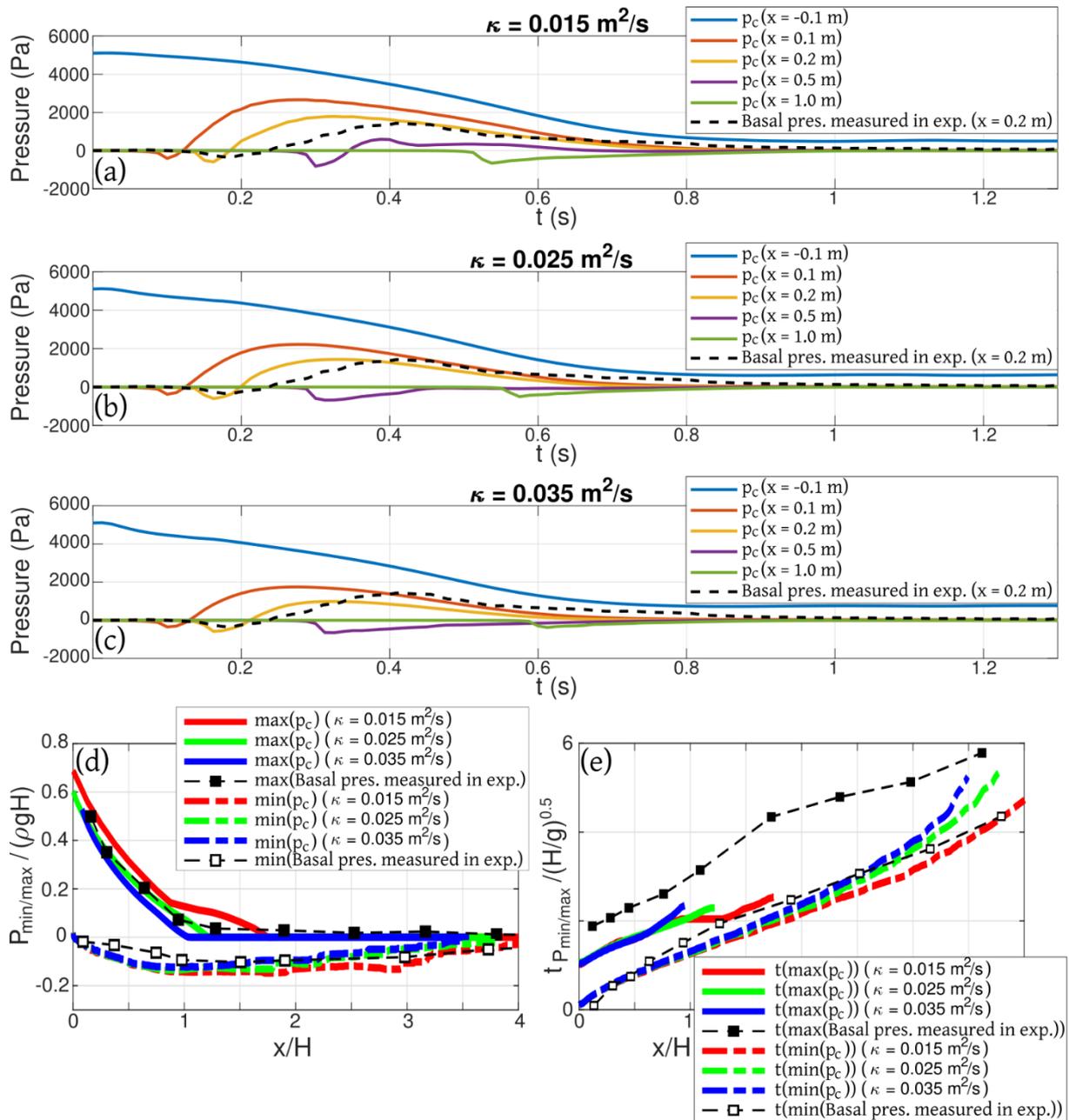
Figure 8. (a-c) Temporal evolution of p_c (see equation (11)) at different positions (see legends)

in simulations performed on horizontal planes, considering initially fluidized conditions and

different values of the effective diffusion coefficient (κ, see titles). Experimental data are also

presented (Roche et al. 2010), which describe the difference between the pressure generated by

the flow above a sensor located at $x = 0.2$ m and the ambient atmospheric pressure. (d)

Maximum normalized values of p_c and differential pressure with respect to the atmosphere in

numerical simulations and in the benchmark experiment, respectively, as a function of

866   horizontal distance (see legend; Roche et al. 2010). (e) Time needed to reach the extreme values

867   (i.e. minimum and maximum values) of p_c and of differential pressure with respect to the

868   atmosphere in numerical simulations and in the benchmark experiment (Roche et al. 2010),

869   respectively (see legend).

870
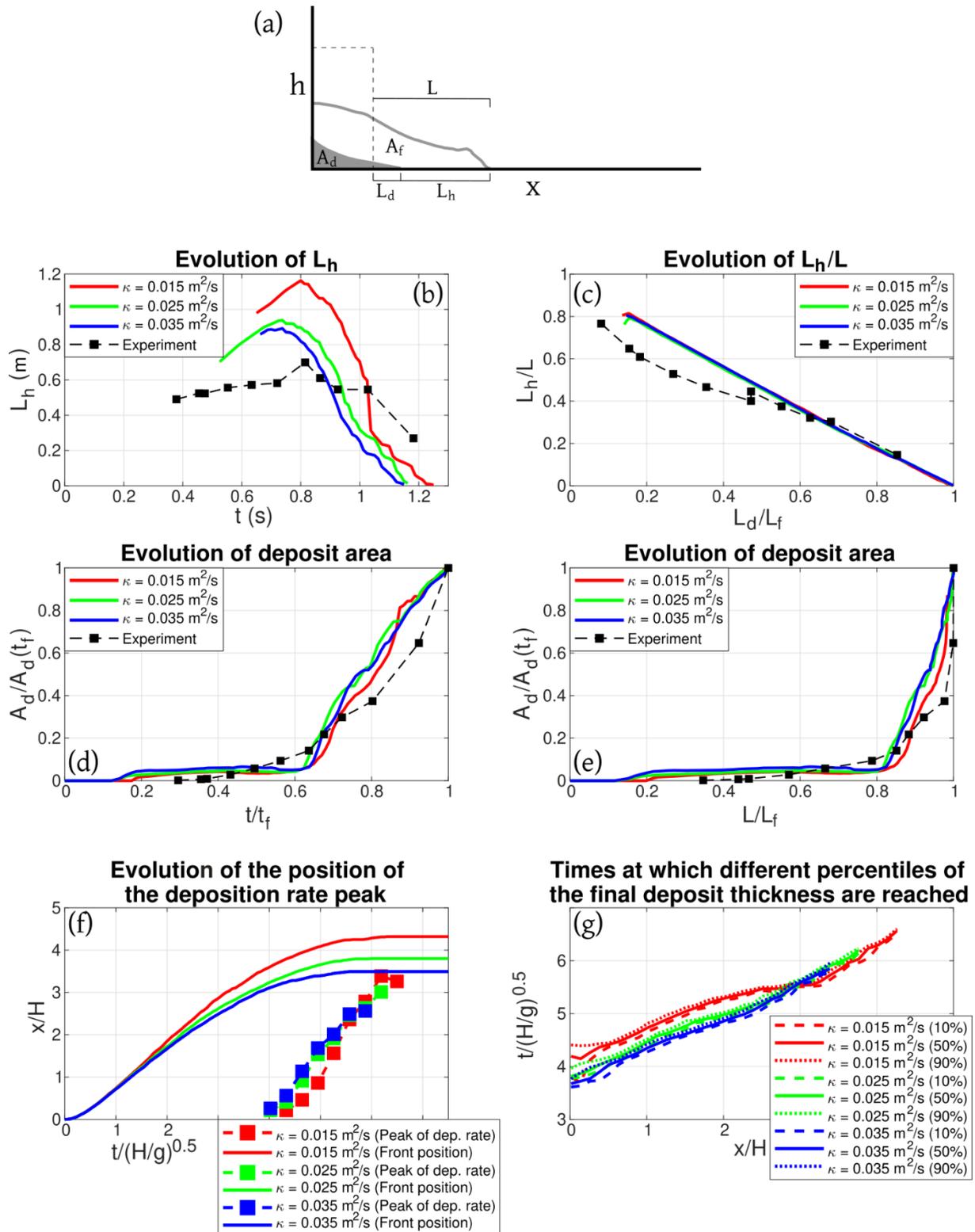
Figure 9. Plots describing the deposition dynamics of particles in our numerical simulations. (a) Schematic figure showing the definitions used to describe the deposition dynamics of the modeled granular flows. (b) Temporal evolution of the sliding head length (L_h, see panel a) in simulations performed on horizontal planes, considering initially fluidized conditions and

876   different values of the effective diffusion coefficient (κ, see legend). (c) L_h/L as a function of

877   L_d/L_f (see panel a) in the same set of simulations, where $L_f = L(t_f)$ and t_f is the final time.

878   (d) Temporal evolution of $A_d/A_d(t_f)$ (see panel a) in the same set of simulations. (e)

879    $A_d/A_d(t_f)$ as a function of L/L_f (see panel a) in the same set of simulations. (f) Temporal

880   evolution of the position at which the peak of deposition rate is modeled in the same set of

881   simulations. The front position is also included. (g) Times at which different percentiles (10%,

882   50% and 90%) of the final deposit thickness are reached as a function of distance along the x-

883   axis, for the same set of simulations. In panels (b)-(e) we include data from the benchmark

884   analogue experiment (Roche 2012).

885

886
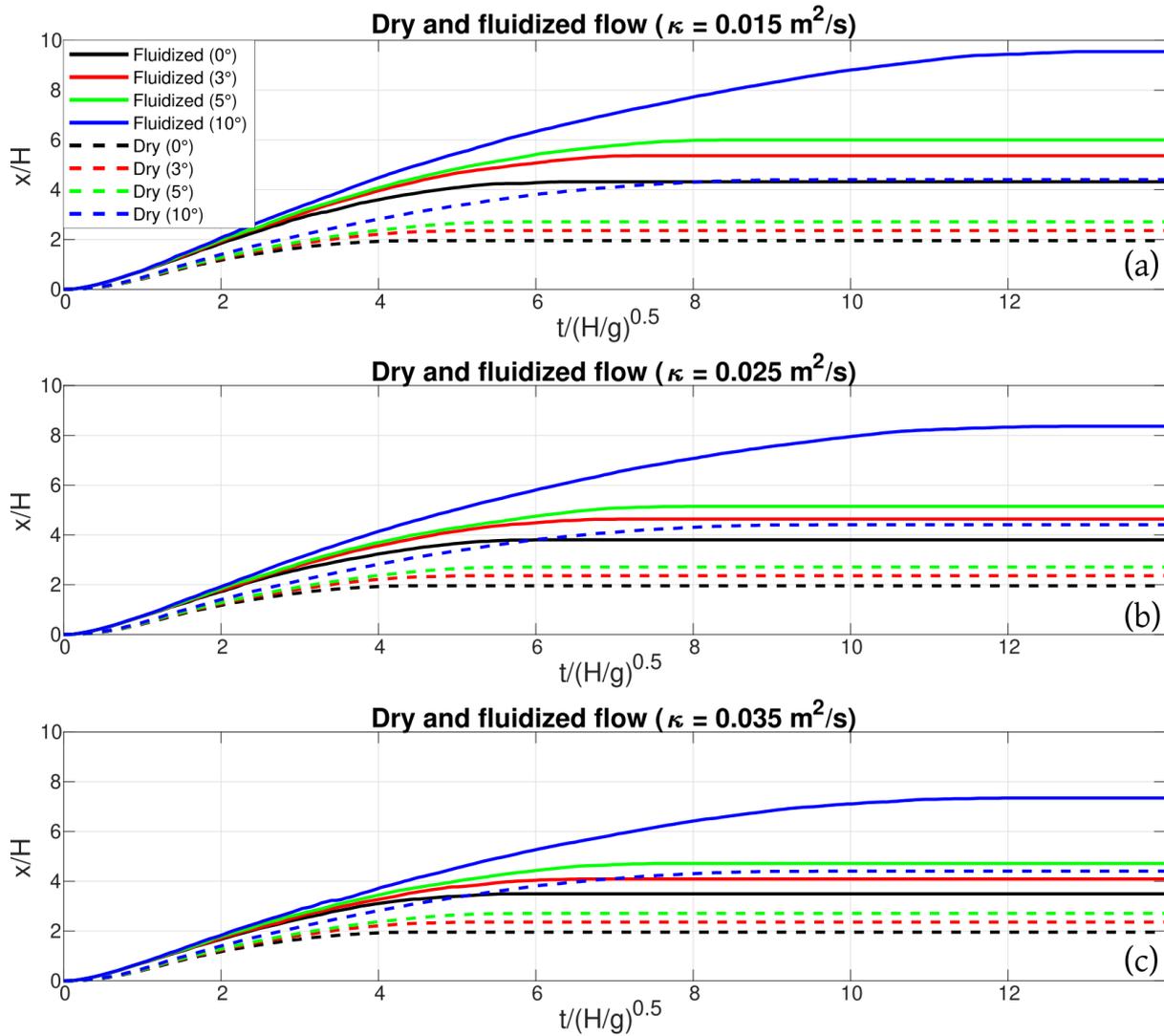
Figure 10. Temporal evolution of the front position of the granular flows in simulations with variable initial fluidization conditions (dry and fluidized flows) and different values of the effective diffusion coefficient and surface slope angle (see titles and legend).
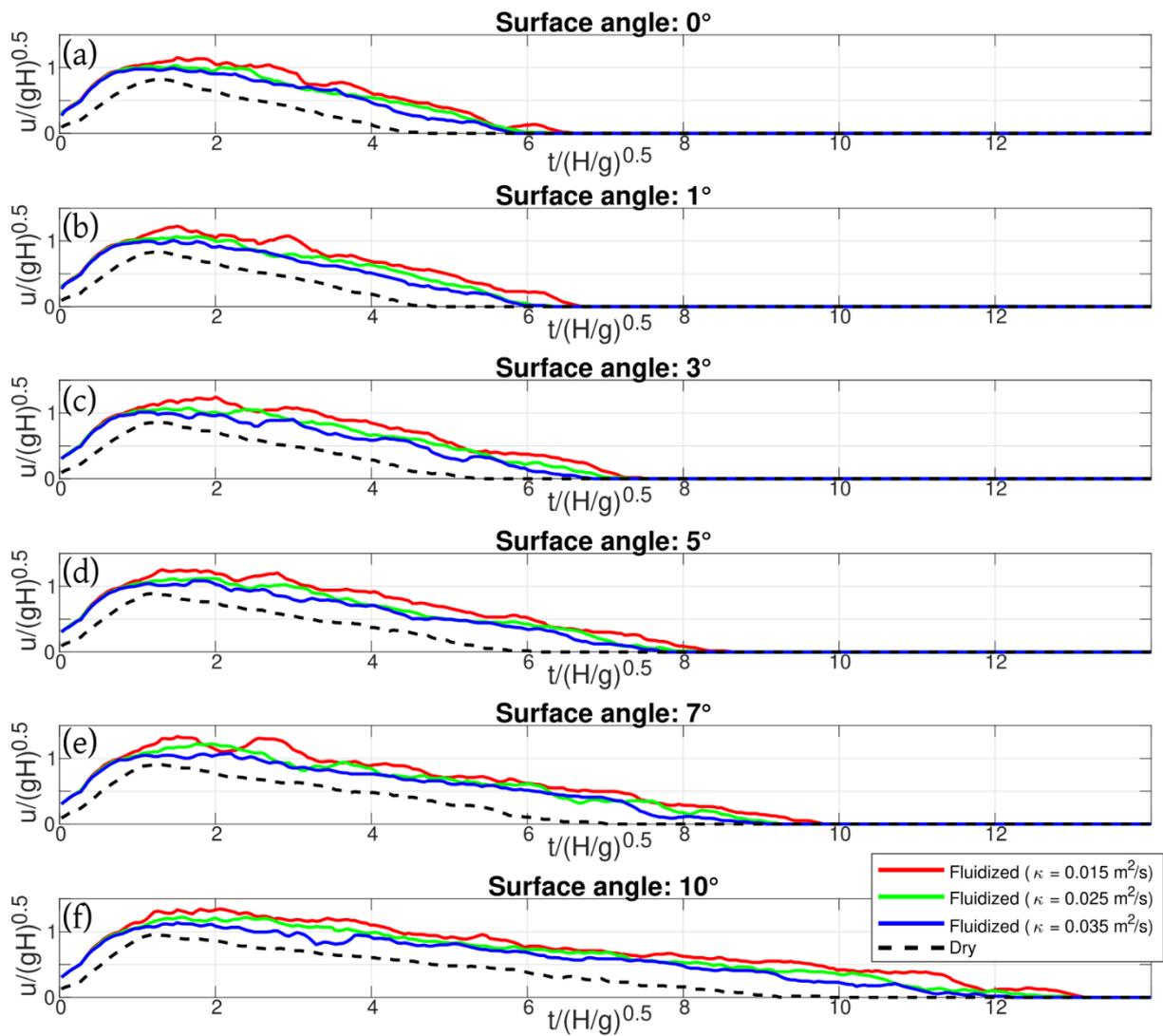
Figure 11. Temporal evolution of the front velocity of the granular flows in simulations with variable initial fluidization conditions (dry and fluidized flows) and different values of the effective diffusion coefficient and surface slope angle (see titles and legend). A moving average function was applied to these curves, considering a time window of 0.1 s.
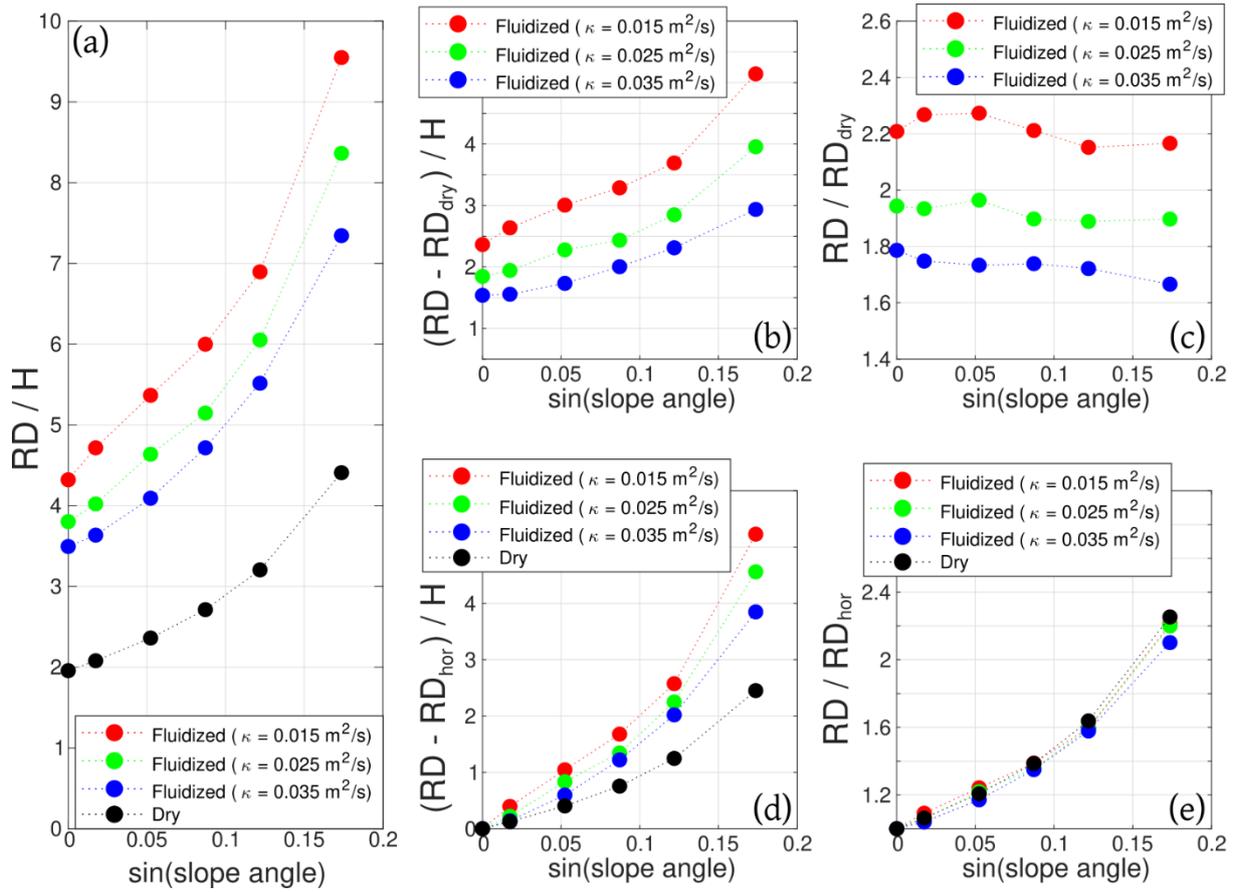
Figure 12. Comparison of the run-out distance of granular flows in simulations performed considering variable initial conditions (dry and fluidized flows) and different effective diffusion coefficients as a function of the surface slope angle. We use the function $\sin(\cdot)$ in the x-axes because it is the driving component of gravity. RD/H: run-out distance over initial column height (H). $(RD - RD_{dry})/H$: increase of run-out distance over H with respect to dry flows. RD/RD_{dry}: ratio of run-out distance with respect to dry flows. $(RD - RD_{hor})/H$: increase of run-out distance over H with respect to a flow propagated over a horizontal surface. RD/RD_{hor}: ratio of run-out distance with respect to a flow propagated over a horizontal surface.

911
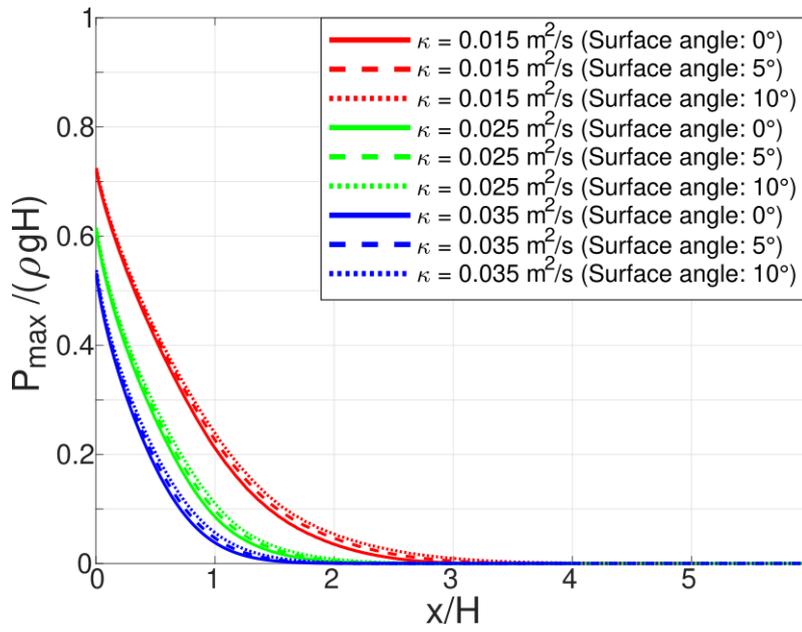
Figure 13. Maximum normalized basal pore pressure during the propagation of fluidized granular flows as a function of horizontal distance in numerical simulations with different effective diffusion coefficients and surface slope angles (see legend).

912

913

914

915

916
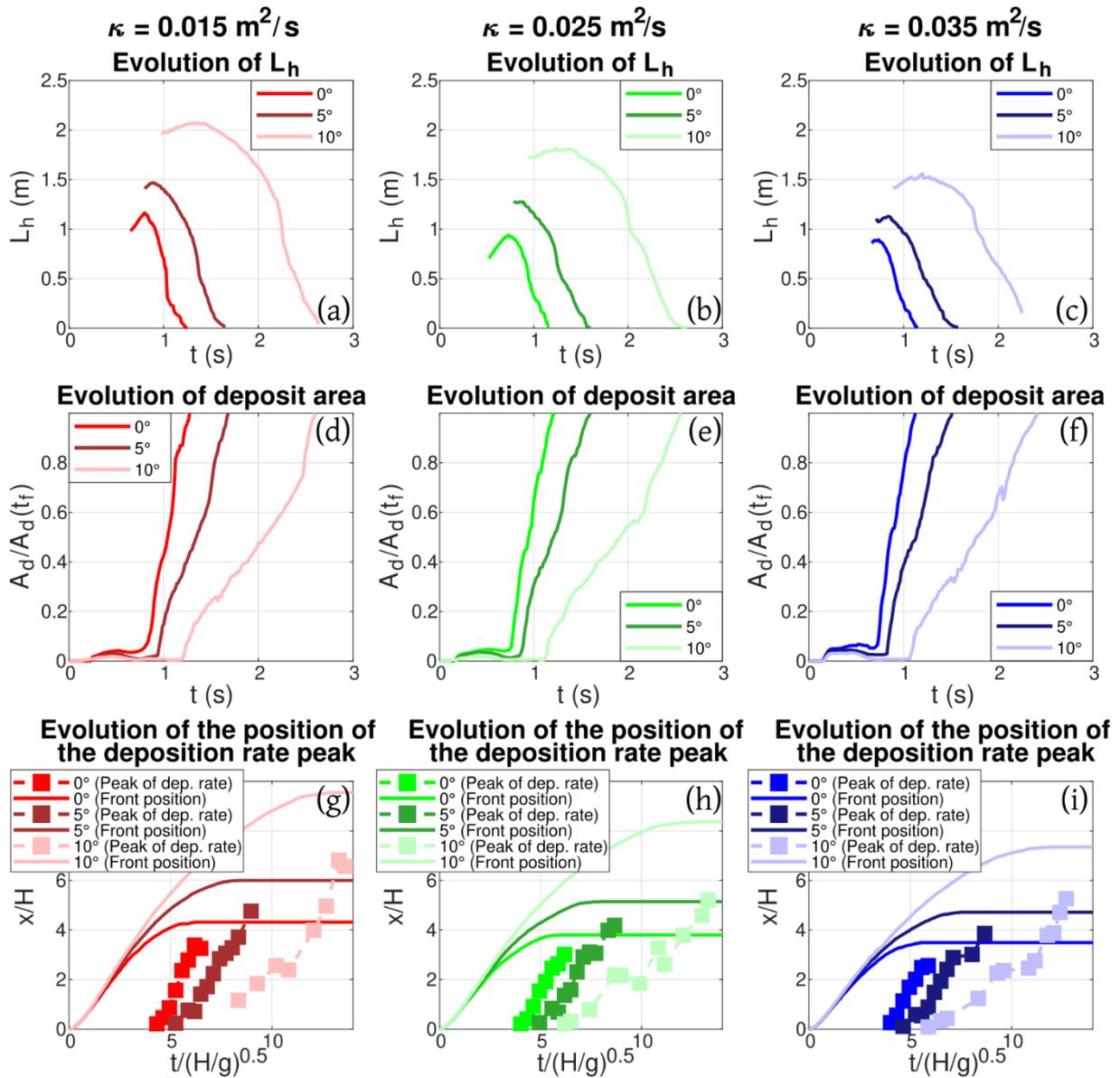
Figure 14. (a-c) Temporal evolution of L_h (see Figure 9a) in simulations performed on horizontal and inclined planes (see legends), considering initially fluidized conditions and different values of the effective diffusion coefficient (κ, see titles). (d-f) Temporal evolution of $A_d/A_d(t_f)$ (see Figure 9a) in the same set of simulations. (g-i) Temporal evolution of the position at which the peak of deposition rate is modeled in the same set of simulations. The front position is also included.